JOURNAL OF GEOPHYSICAL RESEARCH, VOL. 103, NO. E10, PAGES 22,857–22,889, SEPTEMBER 25, 1998

Thermal structure of Jupiter's atmosphere near the edge of a 5-μm hot spot in the north equatorial belt

Alvin Seiff,[1,2] Donn B. Kirk,[3] Tony C. D. Knight,[4,5] Richard E. Young,[6] John D. Mihalov,[6] Leslie A. Young,[7] Frank S. Milos,[6] Gerald Schubert,[8] Robert C. Blanchard,[9] and David Atkinson[10]

Abstract. Thermal structure of the atmosphere of Jupiter was measured from 1029 km above to 133 km below the 1-bar level during entry and descent of the Galileo probe. The data confirm the hot exosphere observed by Voyager (~900 K at 1 nanobar). The deep atmosphere, which reached 429 K at 22 bars, was close to dry adiabatic from 6 to 16 bars within an uncertainty ~0.1 K/km. The upper atmosphere was dominated by gravity waves from the tropopause to the exosphere. Shorter waves were fully absorbed below 300 km, while longer wave amplitudes first grew, then were damped at the higher altitudes. A remarkably deep isothermal layer was found in the stratosphere from 90 to 290 km with T ~ 160 K. Just above the tropopause at 260 mbar, there was a second isothermal region ~25 km deep with T ~112 K. Between 10 and 1000 mbar, the data substantially agree with Voyager radio occultations. The Voyager 1 equatorial occultation was similar in detail to the present sounding through the tropopause region. The Voyager IRIS average thermal structure in the north equatorial belt (NEB) approximates a smoothed fit to the present data between 0.03 and 400 mbar. Differences are partly a result of large differences in vertical resolution but may also reflect differences between a hot spot and the average NEB. At $15 < p < 22$ bars, where it was necessary to extrapolate the pressure calibration to sensor temperatures up to 118°C, the data indicate a stable layer in which stability increases with depth. Consistent with the indication of stability, regular fluctuations in probe vertical velocity imply gravity waves in this layer. At $p > 4$ bars, probe descent velocities derived from the data are consistently unsteady, suggesting the presence of large-scale turbulence or gravity waves. However, there was no evidence of turbulent temperature fluctuations >0.12 K. A conspicuous pause in the rate of decrease of descent velocity between 1.1 and 1.35 bars, where a disturbance was also detected by the two radio Doppler experiments, implies strong vertical flow in the cloud seen by the probe nephelometer. At $p < 0.6$ bar, measured temperatures were ~3 K warmer than the dry adiabat, possible evidence of radiative warming. This could be associated with a tenuous cloud detected by the probe nephelometer above the 0.51 bar level. For an ammonia cloud to form at this level, the required abundance is ~0.20 × solar.

1. Introduction

This paper reports principal results of the Galileo probe atmosphere structure experiment. The primary goal of the experiment was to define the thermal structure of Jupiter's atmosphere below the clouds, a region inaccessible to remote sensing, by direct sensing of atmospheric temperature and pressure during parachute descent to a survivable depth of at least 10 bars. The second goal was to define the structure of the upper atmosphere starting in the exosphere at ~10^{-11} kg/m^3 and continuing to the cloud tops. These would be the first in situ measurements of the atmosphere of Jupiter.

At the time of the proposal (1976), Pioneer 10 and 11 had flown by Jupiter (in December 1973 and December 1974), and the structure of the atmosphere from 10 to 700 mbar had been deduced from infrared radiometry [*Orton and Ingersoll*, 1976] and radio occultation [*Kliore and Woiceshyn*, 1976]. During Voyager flybys, improved measurements of both types were performed over a greater pressure range, 1–1000 mbar [*Kunde et al.*, 1982; *Lindal et al.*, 1981]. Prograde winds with velocities ~85–100 m/s had been measured at the cloud tops at the probe entry site (in the north equatorial belt (NEB)) with occasional bursts as high as 150 m/s [*Limaye et al.*, 1982, 1980; *Beebe et al.*, 1996]. It was our intent to obtain measurements through and well below the clouds, to improve accuracy and resolution, and so to define the atmospheric stability against overturning, observe thermal effects of clouds, detect and quantify turbulence, and make other dynamical observations.

Densities at a few levels in the upper atmosphere were also

[1]Department of Meteorology, San Jose State University Foundation, San Jose, California.
[2]Now at NASA Ames Research Center, Moffett Field, California.
[3]Department of Physics, University of Oregon, Eugene.
[4]Martin Marietta Aerospace, Denver, Colorado (retired).
[5]Now at Lakewood, Colorado.
[6]NASA Ames Research Center, Moffett Field, California.
[7]Center for Space Physics, Boston University, Boston, Massachusetts.
[8]Department of Earth and Space Sciences, University of California, Los Angeles.
[9]NASA Langley Research Center, Hampton, Virginia.
[10]Department of Electrical and Computer Engineering, University of Idaho, Moscow.

Copyright 1998 by the American Geophysical Union.

Paper number 98JE01766.
0148-0227/98/98JE-01766$09.00

Table 1. Entry Mode Data Acquisition

Sensor	Range	Limits, m/s^2	Sampling Interval, s	Nominal Measurement Resolution, m/s^2	Altitude Resolution, km
a_{z1}, a_{z2}	1	0–0.123	0.625	3.0×10^{-5}	4.5
	2	0–3.92		0.00096	4.5
	3	±62.7		0.0306	4.5–0.24
	4	0–4016		0.98	4.5
a_N	1	±0.17	1.0	0.00068	7
	2	±11		0.0435	7–0.5
	3	±177		0.696	7

measured from solar and stellar occultations during Voyager flybys in 1979. Temperatures inferred showed a very hot exosphere, initially reported as 1400 K at 1400 km [*Atreya et al.*, 1979]. At Jupiter's distance from the Sun, solar radiation is insufficient to maintain such temperatures [*Strobel and Smith*, 1973]. Dissipation of gravity waves [*Yelle et al.*, 1996; *L. Young et al.*, 1997] and energetic particle precipitation [*Hunten and Dessler*, 1977; *Waite et al.*, 1997] were proposed as mechanisms for heating the upper atmosphere. Our goal was to define the thermal structure in the upper atmosphere continuously and in detail, to search for evidence of gravity waves, and to obtain evidence, if possible, for the heating mechanism.

Models of Jupiter's interior [e.g., *Hubbard*, 1969; *Smoluchowski*, 1976] treated the temperature structure as adiabatic. From Pioneer 11, Voyager, and Earth-based data, it was known that Jupiter radiates more energy to space than it receives from the Sun [*Ingersoll et al.*, 1975; *Hanel et al.*, 1981], and this energy must be transported from the planet's interior. Convective transport requires nearly neutral, as opposed to stable, thermal structure. But recent studies have indicated the possibility of stable layers in the atmosphere [*Flasar and Gierasch*, 1986; *Ioannou and Lindzen*, 1993a, b; *Guillot et al.*, 1994], wherein radiative transport dominates. Horizontally propagating wave packets recorded in Voyager images [*Flasar and Gierasch*, 1986] are evidence of stability at the level of the upper clouds. In the absence of water, as in a 5-μm hot spot [*Bjoraker et al.*, 1986; *Carlson et al.*, 1996], *Guillot et al.* [1994] argue that radiative transport could dominate between the 200 and 400 K levels, creating a stable layer. Also, a stable layer within Jupiter was required to provide internal dissipation in the gravitational interaction between Io and the planet [*Ioannou and Lindzen*, 1993] sufficient to allow the orbit of Io to evolve to its present distance from Jupiter. Hence the possibility was raised of a stable layer or layers within the experiment regime.

Nevertheless, the preencounter expectation was for an adiabatic atmosphere, possibly wet-adiabatic in the clouds, with three cloud layers, an upper cloud of ammonia crystals with its base at 700 mbar, a water cloud (mostly water ice) with its base at 5 bars, and an intermediate cloud of ammonium hydrosulfide [*Lewis*, 1969]. However, the probe entered near the edge of a 5-μm hot spot [*Orton et al.*, 1996, this issue], a region bright in the infrared because it is relatively cloud free, and with low water content [*Bjoraker et al.*, 1986]. This altered the expectation with respect to clouds and water.

This paper will summarize results to date of the probe atmosphere structure experiment. Many of its goals were realized. Some were partly frustrated because probe internal temperatures far exceeded their expected range [*R. Young et al.*, 1996]. Pressure and temperature data were successfully acquired in the deep atmosphere to the 22 bar level. The data were used to investigate atmospheric stability, to derive altitudes and descent velocities. The latter were necessary to the determination of horizontal wind velocities from Doppler data [*Atkinson et al.*, 1996, 1997, this issue]. The measurements also provided a depth scale for other probe experiments. Accelerations in descent were used to determine horizontal winds [*Seiff et al.*, 1997b] and turbulence. The upper atmosphere experiment fully realized its goals. The atmosphere was well characterized from the nanobar level to the cloud tops.

Preliminary reports of the experiment results have been published [*Seiff et al.*, 1996a, 1997a]. The instrument was described by *Seiff and Knight* [1992]. We first review the experimental approach, the data obtained, and their accuracy. We then outline the data analysis methods and present the derived atmosphere structure. We close with a discussion of the results and some implications.

2. Experimental Approach, Sensor Accuracy, and Resolution

2.1. Experiment Design

To set the stage for presentation of the data acquired, we briefly review the design and operation of the Atmosphere Structure Instrument (ASI). The instrument operated in two basic modes. First, during high-speed entry of the probe into the atmosphere, sensitive accelerometers detected and recorded decelerations for 240 s. Since the communication link was not then established, the data were stored in probe memory and were read out twice during the descent. Two components of acceleration were read, along and normal to the z axis (the probe axis of symmetry), which was approximately aligned with the flight direction. The axial component was redundantly sensed by independent sensors designated z_1 and z_2. Multiple sensor ranges, shown in Table 1, permitted high measurement resolution over a dynamic range of 10^8. Sampling period was 5/8 s for the z axis sensors (Table 1). Altitude resolution was ~4.5 km during the period of high velocity, improved to ~0.25 km just before parachute deployment. Readings from the two sensors were interdigitated, so that if used as a single data set, they provided altitude resolution ranging from ~2.25 to 0.12 km. Accelerations normal to the z axis were sampled at 1 s intervals, primarily to define probe angle of attack. Sensor and electronics temperatures were read every 40 s.

A few seconds before parachute deployment, the instrument

Table 2. Descent Mode Data Acquisition

Sensor	Range	Sampling Interval, s	Nominal Measurement Resolution	Altitude Resolution, km
T_1	0–520 K	4	0.12 K	0.36–0.11
T_2	0–560 K	4	0.13 K	0.36–0.11
p_1	0–500 mbar	4	0.5 mbar	0.36
p_2	0–4 bars	4	4 mbar	0.36–0.18
p_3	0–28 bars	4–2	28 mbar	0.36–0.11
ΔV_{z1}	1003 m/s	16	0.49 m/s	1.4–0.5
ΔV_{z2}	1003 m/s	16	0.49 m/s	1.4–0.5
a_N	0–11 m/s^2	16	0.0435 m/s^2	1.4–0.5
a'_z	0–4.63 m/s^2	96	0.58 m/s^2	8.4–3
a'_N	0–0.47 m/s^2	96	0.04 m/s^2	8.4–3

descent mode was initiated on spacecraft command. In descent, primary measurements were pressure and temperature, but summary acceleration data were also transmitted in both the z and normal-to-z (N) axes. Excursions from the mean accelerations were also sampled as a measure of turbulent fluctuations.

A brief preentry calibration (pec) (419 bits of data) was performed and stored in memory ~15 min before the expected atmosphere encounter to establish the basic health of the instrument and to record precisely the preencounter zero readings of pressure sensors and accelerometers on all ranges. Sensor temperatures also were read as well as values of standard voltages and analog to digital (A/D) converter offsets and calibrations against a precision voltage source. This information was transmitted twice during parachute descent. It showed that the instrument was in good health, with no evidence of degradation in performance as a result of having passed through the Jovian radiation belt.

The probe telemetry rate was 128 bits/s, of which the ASI allocation was 18 bits/s. Over 3550 s of descent, the total ASI data quantity was thus ~64 kbit. The 18 bits/s data rate dictated a very spare sampling strategy. Data sampling in this mode is summarized in Table 2. Temperatures were measured every 2 s, alternating between two sensors. Pressure measurements were simultaneous within milliseconds with temperatures. At $p < 4$ bars, the two most sensitive on-scale pressure sensors were read alternately. At $p > 4$ bars, only the highest range sensor was on-scale, and it was sampled every 2 s. Each z axis accelerometer was read 32 times/s in descent, but the data rate could support only one sample every 16 s. The readings were therefore summed over 512 samples to provide the integrated velocity change ΔV_z transmitted with 11-bit resolution every 16 s. Integration remainders were carried forward to the next sample to preserve high accuracy in the cumulative velocity loss. Integration intervals of the two axial sensors were offset by 8 s to provide a sample every 8 s. Lateral accelerometer data transmitted every 16 s were the sum of 512 samples truncated to 8 bits. Minimum and maximum values sensed during the integration period were also sampled. Turbulence measurements, designated in the Table by a'_z and a'_N, were derived from the accelerometer data by counting the number of crossings of a set of predetermined "threshold" levels distributed about the mean. Counters were incremented each time an accelerometer output (each sampled at 32 Hz) crossed a threshold in a positive direction. These data were collected from one z axis sensor and the normal-to-z, N axis sensors. Perturbation crossing levels will be indicated in the turbulence data presentation. To allow for slight variations in sensor calibrations with temperature, individual sensor and electronics temperatures were measured in descent once/major frame (every 64 s).

2.2. Sensor Stability, Calibration, and Accuracy

The ASI sensors were provided by vendors, the accelerometers by Bell Aerospace, the pressure sensors by Tavis Corporation. The atmospheric temperature sensors were built to our design by Rosemount, Inc. The ASI electronics were designed and built by Martin Marietta Aerospace (now Lockheed-Martin). Sensors were initially calibrated by the vendors before delivery. They were recalibrated repeatedly at Ames Research Center up to the time of final delivery of the instrument to the spacecraft contractor in order to evaluate long-term stability of calibration. Calibration activities were described by *Seiff and Knight* [1992]. A broad summary of calibration activities follows, together with supplementary information developed following initial analyses of the data obtained in the Jovian atmosphere.

The four accelerometers were calibrated against the precisely known gravity field of Earth. Sensors were rotated through 360° on a precision dividing head to expose them to inputs from 0 to ±1 g, where g is Earth's gravity acceleration. Data taken were used to define both the sensitivity (scale factors) and zero-input offset readings on each sensor range. Bell Aerospace company performed these calibrations over a temperature range from −20° to +50°C, the expected temperature limits in descent in Jupiter's atmosphere. The sensor responses to acceleration are linear by virtue of their operating principle [*Seiff and Knight*, 1992]. This was verified in a test at 410 g by use of precisely known electrical currents to simulate an acceleration input. This confirmed the 1 g calibration to three significant figures. A centrifuge test of the complete instrument was performed to simulate the entry profile to a peak of 210 g. This test also verified the calibrations to within the accuracy of the centrifuge.

How stable were the calibrations? On the 6.5 g full-scale range (range 3) used in Jupiter descent, scale factors of the two axial sensors repeated over a period of years to better than 0.03% at a given temperature. On the most sensitive range, 3.1 μg/count, scale factors repeated to better than 0.4%. The long-term stability of the zero offsets was about 150 μg on all ranges. In parachute descent at Jupiter, probe internal temperatures exceeded both the −20° and +50°C expected limits and varied rapidly. The rate of temperature change of the accelerometers was sufficient that its effect on the calibrations

had to be assessed. Test data acquired at Bell Aerospace at temperature rates from −1.2 to +1.3°C/min were extrapolated to temperature rates experienced in flight, −5° to +4°C/min to make corrections of ~1 count.

The three pressure sensors were calibrated by exposing them to constant pressures determined by standard precision pressure measuring equipment (Mensor pressure sensors), which were calibrated against accurately known masses (dead weight test apparatus). Calibrations performed at four temperatures between −20° and +50°C defined scale factors and variations with temperature of the zero offsets, as well as deviations from linearity. These efforts showed scale factors typically to be repeatable within 0.1% at a constant temperature, and to vary <0.5% over the −20° to +50°C range [*Seiff and Knight*, 1992]. The zero offsets were found to vary by up to 0.5% of full scale over this temperature range and to be repeatable to within 0.2%. At the time of Jupiter entry, offsets were read in the preentry calibration 15 min before entry. Since it was known that the sensors would be exposed to temperature variations during descent, the output sensitivity to the rate of change of the sensor temperature was determined [*Seiff and Knight*, 1992]. During descent into the Jovian atmosphere, it was found that the rate of change of sensor temperature exceeded the calibration range, particularly early in the descent, where the probe was being rapidly cooled by the atmosphere. A series of simulation tests of the flight spare and engineering unit sensors was carried out in 1996 to provide a basis for correcting the pressure data for these conditions. These tests are described in Appendix B.

The atmospheric temperature sensor was a dual-element platinum resistance thermometer, modeled after the sensor we had used to measure the lower atmosphere of Venus [*Seiff et al.*, 1980]. The primary element, T_1, was a free-wire sensor, a platinum wire 0.1 mm in diameter wrapped around an open, planar platinum-rhodium frame [*Seiff and Knight*, 1992]. The secondary element, T_2, was a 25 μm Pt wire bonded over a thin layer of glass insulation on the forward surface of the outermost tube of this frame. The two elements were calibrated together a number of times over a period of years using standard temperature baths, boiling nitrogen (77.4 K), oxygen (89 K) and water (373 K), and freezing water (273.15 K), all under atmospheric conditions [*Seiff and Knight*, 1992]. The calibrations were related to the International Practical Temperature Scale (1968) based on the electrical resistivity characteristics of platinum, which provides a precise basis for interpolation and extrapolation of the calibration data. To protect the sensor from shorting and electrical discharge in Jupiter's clouds, it was coated, first, with an insulating polymer, parylene (thickness 25 μm), and then with 2.5 μm of gold to conduct electrical discharges encountered in descent into the probe. The coatings caused a small calibration shift, but several calibrations of the coated sensor showed good repeatability. It was possible to repeat primary element calibrations in boiling nitrogen with a standard deviation of 0.02 K, and in freezing water with a standard deviation of 0.07 K [*Seiff and Knight*, 1992]. With calibration, extrapolation, interpolation, and digitization uncertainties considered, overall measurement uncertainty was from 0.1 K at 100 K to ~1 K at 500 K.

The sensors were further tested at $T > 373$ K in a small, closed-circuit flow channel of 6-inch nominal diameter, developed for this purpose. The air temperature in this channel was controlled to simulate temperature histories similar to those expected on Jupiter, ranging from room temperature to 480 K.

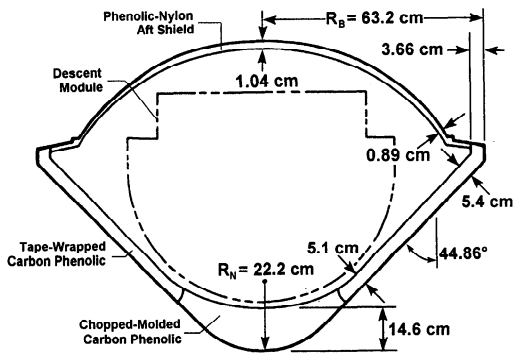

Figure 1. Geometry of the Galileo probe, showing heat shield thickness and outline of the descent capsule.

Readings from the two sensor elements were found to agree in these tests to within 0.25 K typically, and to agree with colocated accurate thermocouples to within tenths of a degree. Nonuniformity of the test stream temperature was of this order. No operational difficulties were encountered in these tests or in Jupiter descent. The sensors were also tested to evaluate conduction errors for situations in which the mounting surface was at temperatures as much as 50°C different from atmospheric temperature. Conduction errors were found to be below the threshold of measurement, ~0.01 K.

2.3. Probe Factors: Mass Loss

Since the probe shape determines the drag coefficient, and its mass and frontal area determine the deceleration at a given atmospheric density, the probe itself is a part of the experiment. Mass loss and shape change during heat shield ablation affect the subsequent response to atmospheric density.

Figure 1 shows a cross section of the Galileo probe at entry. The heat shield was a cone of 44.86° half-angle with a spherical nose 22.2 cm in radius. The radius of curvature of the spherical aft cover was 62.08 cm. The dashed outline shows the descent capsule nested within the heat shield. At the start of descent, the aft cover was discarded, the parachute was deployed, and the heat shield was jettisoned to fall away from the parachute-supported descent module.

Figure 2 shows the original heat shield and the shape change at the end of ablation, as indicated by 10 ablation sensors embedded in the heat shield (Appendix A) [*Milos*, 1997]. Only ~30% of the thick cap at the stagnation point was ablated away by the entry heating, while at the conical base, ~74% of the thickness was ablated. Resulting changes in mass and frontal area were accounted for in the data analysis.

Parameters of the entry at 450 km altitude above the 1 bar level are given in Table 3 and compared with those expected. The entry was shallow by 0.2°, but well within the targeted band. The helium fraction of the two bulk constituents, 0.136, determined by the probe helium abundance detector [*von Zahn and Hunten*, 1996; *von Zahn et al.*, this issue] and the neutral mass spectrometer [*Niemann et al.*, this issue], was greater than in the nominal preflight atmospheric model, but the entry was less severe than the worst case.

The surface recession was sensed by 10 ablation sensors located at six distances from the nosetip, where shown by the black diamonds in Figure 2. At three body stations, two sensors were located on opposite sides of the body to check for symmetry. These stations were (1) on the nose, (2) at a station

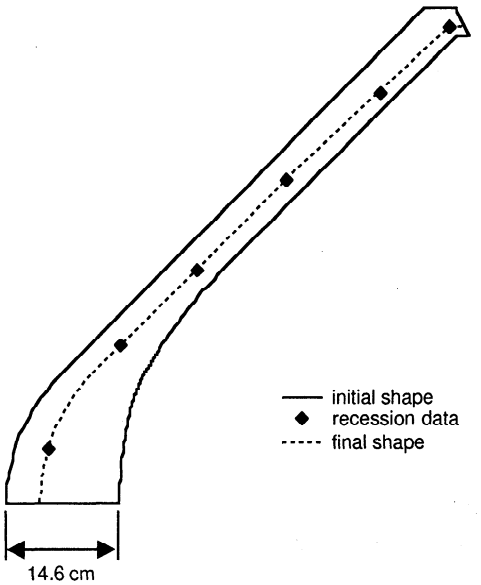

Figure 2. Heat shield cross section before and after ablation. Symbols indicate locations of ablation sensors.

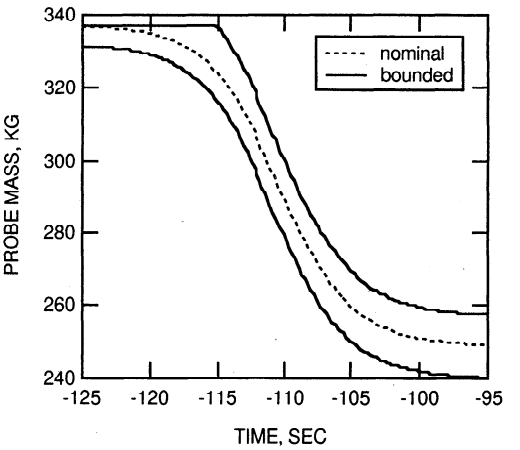

Figure 3. Mass of the probe as a function of time in seconds before the start of descent, during the period of intense ablation determined from ablation sensors, with upper and lower limits.

along the conical surface, and (3) on the maximum diameter ring at the base. The data showed that the ablation was symmetric within measurement accuracy. Nominal curve fits and bounds for axisymmetric recession were obtained as functions of time for the six locations on the vehicle forebody. The frontal area history was obtained directly from the curve fit to the diameter recession data. The probe shape history was calculated from the six recession curve fits, and the mass history (Figure 3) was derived from the shape history. Upper and lower limits were derived to the mass loss based on uncertainties in the recession measurement.

The total recession was 4.45 ± 0.25 cm at the nose, a minimum of 2.74 ± 0.15 cm at midfrustum, and 4.00 ± 0.15 cm near the base of the cone. The total forebody ablation mass loss was 79 ± 4 kg. The base radius decreased 2.58 ± 0.15 cm, which corresponds to decrease of 8.0 ± 0.5% in base area. The final shape can be approximated by a sphere-cone with 23.5 cm nose radius and 44.0° half-angle.

There was additional ablative mass loss from the aft-cover heat shield, estimated to be 8.4 ± 4.2 kg, and from subsurface pyrolysis of the heat shields, estimated to total 1.5 ± 0.5 kg [*Milos*, 1997]. Combining these with the forebody ablation mass loss, with uncertainties directly added, the total mass loss is 88.9 ± 8.7 kg, and the final probe mass, 250.0 ± 8.7 kg, a formal uncertainty of ±3.5%. The uncertainty begins at the start of ablation, −120 s, and is maximum after $t = -100$ s, when ablation ends (Figure 3).

The mass at the end of entry was independently assessed by examining the match of atmospheric densities at experiment mode change from entry to descent. These densities are completely independently determined. An almost exact match occurs with the upper limit mass loss, 97.60 kg. The time history of mass loss during ablation was therefore modeled to move from the entry mass of 338.93 kg to an end point mass of 241.33 kg along a curve similar in shape to the dotted curve in Figure 3.

Table 3. Galileo Probe Entry Conditions

	Preflight Nominal	Actual
Entry velocity, km/s	47.8	47.4054
Entry path angle, deg	−8.6 ± 1.4	−8.4104
Entry latitude, deg		6.5303
Entry longitude, deg		4.9403
Entry heading, clockwise from east, deg		2.6111
Entry angle of attack, deg	7	5.7
He, mol %	11	13.6 ± 0.3
Spin rate, rpm	10.5	10.5
Entry mass, kg	338.93	
Entry diameter, cm	126.49	

2.4. Aerodynamics

To derive accurate densities in Jupiter's upper atmosphere from deceleration measurements requires accurate knowledge of the probe drag coefficient. Experimental and theoretical studies of the Galileo probe aerodynamics in hypervelocity flight were made in the years preceding encounter [*Seiff et al.*, 1996b]. Three regimes were studied: the low-density regime where the molecular mean free path is comparable to or greater than the body size and the governing parameter is the Knudsen number Kn; the low-density, hypersonic continuum flow regime, governed by the Reynolds number Re; and the high-Re hypersonic, supersonic, and subsonic regimes with essentially constant Re, where Mach number governs. Figure 4 shows the dependence of drag coefficient on these parameters in each regime.

In the low-density regime (Figure 4, top) $C_D = 2.06$ at the free-molecular limit. There is a protracted transition to continuum flow, which is nearly complete at $Kn \sim 0.01$, $C_D \sim 1.15$. These values of C_D were obtained by Monte Carlo analysis of the motion of individual molecules colliding with the body and with each other [*Haas and Milos*, 1995]. The middle graph in Figure 4 shows the hypersonic C_D as a function of Re, determined experimentally by firing small models of the Galileo probe in a ballistic range [*Intrieri and Kirk*, 1987] and also computationally by numerical solution of the equations of motion, using the methods of computational fluid dynamics (CFD) [*Seiff et al.*, 1996b]. The bottom graph shows $C_D(M)$ at $Re \sim 10^6$, defined by experiment and by CFD

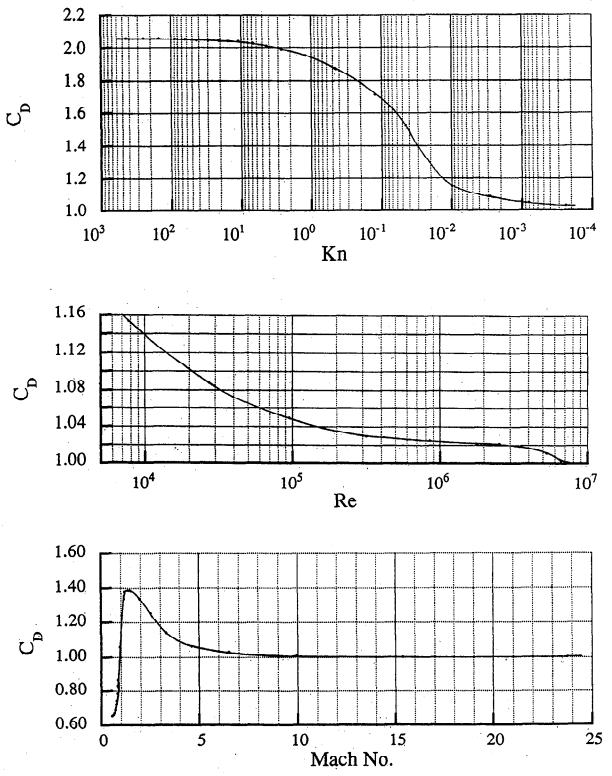

Figure 4. Drag coefficients of the Galileo probe in three flow regimes: (top) the free molecular flow regime and transition to continuum flow, (middle) the low Reynolds number hypersonic regime, and (bottom) the high Reynolds number regime at Mach numbers from 25 to 0.5.

computations for Mach numbers Ma from 25 to 0.5. The heat shield mass loss occurs in this regime, so C_D was determined for the ablated as well as the entry configuration, but changed very little. C_DA during ablation was varied from the initial to the terminal value in proportion to the probe mass variation with time.

Except in the transonic flow regime, the accuracy of these numbers is believed to be ~1 or 2%, as indicated by repeatibility of the ballistic range measurements. The CFD accuracy is somewhat harder to quantify but agreed with experiment within this order of accuracy except near a $Ma = 1$, where there were disagreements ~5%. These are attributed to the fact that the CFD calculations may not have included a wide enough array of grid points. (Subsonic influence of the body extends to infinity, and adequate extent of the calculation grid has not been verified by convergence of the transonic solutions.) Transonic experiments are also possibly subject to wall reflection effects.

To calculate angles of attack during entry, we made use of the ratio of probe normal to axial force coefficients determined experimentally from the hypersonic tests in a ballistic range [*Seiff et al.*, 1996b]. This ratio is identical with the ratio of normal to axial accelerations and varies linearly with angle of attack at small angles of attack. For hypersonic continuum flow this ratio is $a_N/a_z = 0.015\alpha$ for the Galileo probe, where α is the angle of attack in degrees.

The drag coefficient of the probe descending on the parachute was measured in a parachute development test on Earth (reported by *General Electric Co.* [1983] to the probe managers at Ames Research Center). Based on three values obtained at altitudes of 9.1, 6.1, and 4.6 km in Earth's atmosphere, $C_DA = 5.43 \pm 0.17$ m^2 (±3%). In this test, probe and parachute configuration and mass were simulated. Dynamic pressures in equilibrium descent are proportional to g, so were roughly 0.4 of those on Jupiter. Taking into account viscosity differences between the atmospheres, Re based on parachute diameter were ~$\frac{1}{3}$ those on Jupiter. Drop velocities were 21–43 m/s, comparable to those in Jupiter descent. These values are less well determined than the hypersonic drag coefficients.

3. Data Received

3.1. Temperatures

Temperatures measured in descent by the primary T_1 sensor are shown in Figure 5 as a function of time. (Zero time throughout this paper is at the start of the first minor frame of data in the descent mode, designated minor frame 0.) The full set of data points is shown with no line through the points. The fact that the data show little scatter, typically <1 count, implies the absence of turbulent temperature fluctuations >0.12 K. Sensor response times τ and descent velocities V define detectable scales $Z > \tau V$. Initially, the free-wire sensor response time was ~14 ms and the descent velocity ~100 m/s, giving $Z > 1.4$ m. At the end of descent, the response time was 4 ms and the descent velocity ~30 m/s, giving $Z > 0.12$ m.

No prominent steps or slope discontinuities, which might occur on entering or emerging from clouds, are evident. Enlarged sections of the record (Figures 6a and 6b) show where ammonia and water cloud bottoms were expected for solar abundances of nitrogen and oxygen. In Figure 6b, T_1 is high, relative to surrounding readings, between 272.5 and 273.2 K by 0.15–0.2 K. This persists for three consecutive readings, more than 6 s, over an altitude interval of 300 m. T_2 does not show a similar offset. This T_1 temperature offset is unique in the data set. Notice that none of the preceding or following six data points lies this far off the line through the data. The temperature elevation could be the detection of a detached water-ice cloud segment, warmed by particle radiative absorption. However, no unusual signal was detected by the probe nephelometer during this interval (B. Ragent, private communication, 1998). We will discuss other possible evidence of clouds in the temperature data in a subsequent section.

Figure 6 also shows the systematic differences between the

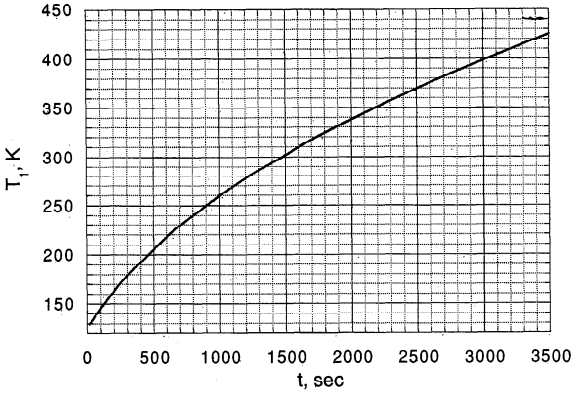

Figure 5. Temperature data from the primary, free-wire sensor in descent on Jupiter. There is no curve through the data points.

free-wire T_1 and the bonded T_2 temperature sensors. They differed systematically by 0.2–0.4 K over the descent. These differences were also seen in ground tests and cruise checkouts and correspond to a combined resistance discrepancy of 0.009–0.020 ohm. They are attributed either to calibration limitations or to a constraining or thermal effect of the tubing to which T_2 is bonded. The differences between sensor readings in Figures 6a and 6b are typical. Most of the results which follow use T_1 because it is better coupled to the atmosphere, free from the tubing support effects, and has faster time response.

Data at the start of descent are shown in Figure 6c. Parachute deployment and heat shield jettison times are marked. The first six temperature readings were taken within the entry probe or behind the heat shield and are not included in Figure 5. When the probe aft-cover was removed at 5 s, temperatures dropped rapidly, and at $t = 16$ s, when the descent capsule was fully exposed, the first atmospheric temperature recorded was 129 K.

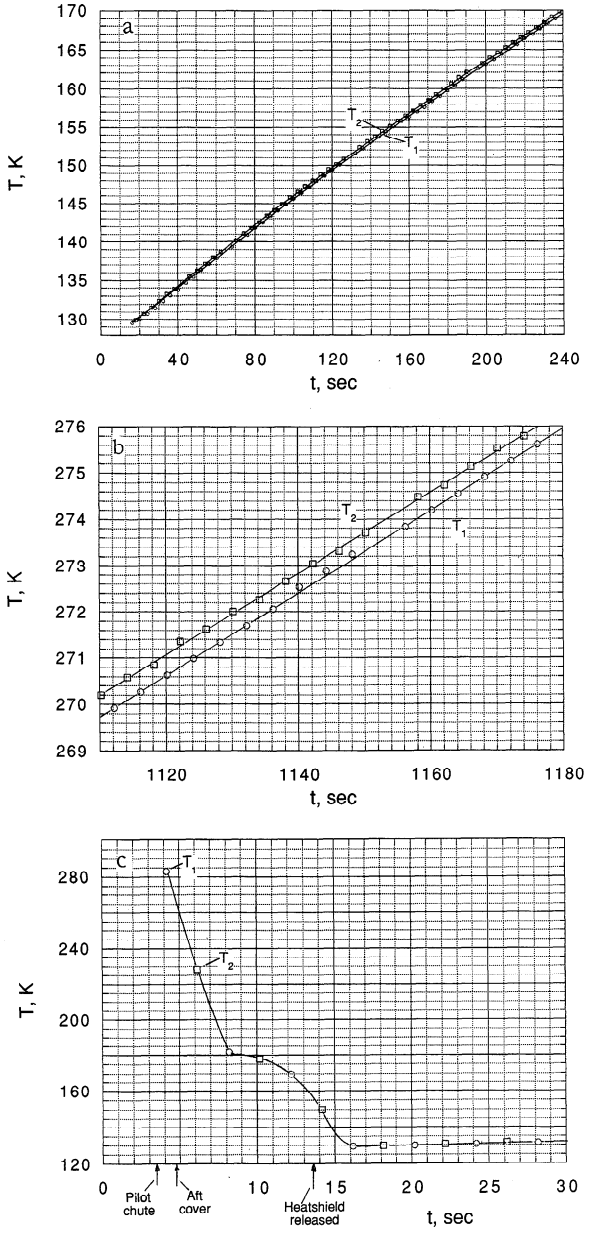

Figure 6. Enlarged segments of the temperature data (a) through the level of the expected NH_3 cloud base, (b) through the level of the expected H_2O cloud base, and (c) in the first 30 s of descent.

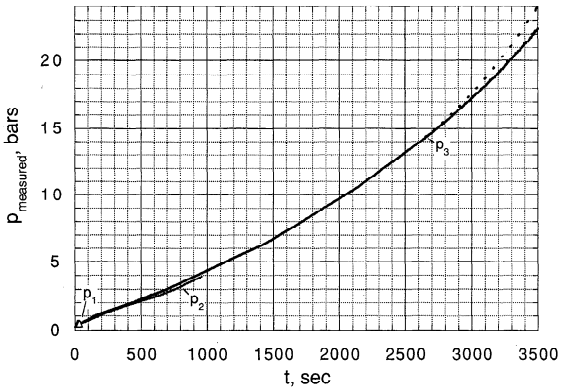

Figure 7. Pressure data from the probe in descent, as received.

There are no known problems with these data. The only possible probe internal temperature effects were on amplifier gain and on the stimulus current, used to convert sensor resistance to a voltage signal. The stimulus current and the amplifier gain were checked periodically during descent by substituting a precision resistor within the electronics for the temperature sensor. When corrected for the small temperature sensitivity of the precision resistor and for offset variations measured in flight, these checks indicated that the electronics were stable within 1 count, or 0.125 K, throughout the descent.

3.2. Pressures

Pressures measured in descent are shown as a function of time in Figure 7. Data are from three independent sensors of increasing range: p_1 (0–500 mbar), p_2 (0–4 bars), and p_3 (0–28 bars). Descent mode, intended to start at the 100 mbar level, was commanded late at an atmospheric pressure near 400 mbar [*R. E. Young et al.*, 1996], when the p_1 sensor was nearly off scale. The p_1 and p_2 sensors were read alternately at 2 s intervals for 32 s to a final $p_1 = 0.474$ bar. The mid- and high-range sensors were read alternately at 2 s intervals to a pressure level of 3.9 bars ($t = 960$ s). Above 4 bars, the high-range sensor was read every 2 s to 22.3 bars at the end of mission ($t = 3502$ s).

The first 100 s of data are shown in Figure 8. The first p_2 reading, 343 mbar, measured probe internal pressure before the aft-cover was removed. When the aft-cover was released, the rapid in-rush of gas contributed to the increase in measured pressure. The high descent velocity before parachute deployment, 438 m/s at $t = 0$, also made for a rapid increase in pressure. At this descent velocity and for $\rho = 0.088$ kg/m^3, the rate of pressure increase given by $dp_{atm}/dt = (dp/dz)(dz/dt) = -\rho g\, dz/dt$, is 8.95 mbar/s. The observed initial dp/dt is 19.5 mbar/s. The difference is the rate of pressure increase due to atmospheric inflow.

At $p < 500$ mbar, the p_1 and p_2 readings differed by up to ~10 mbar, or >2 counts of p_2. They had been expected to agree within 1 count or 4 mbar. The larger disagreement is attributed to the high rate of temperature change, −4.5°C/min, imposed on the sensors within seconds of the start of descent (see below). The temperature rate correction to p_2 (Appendix

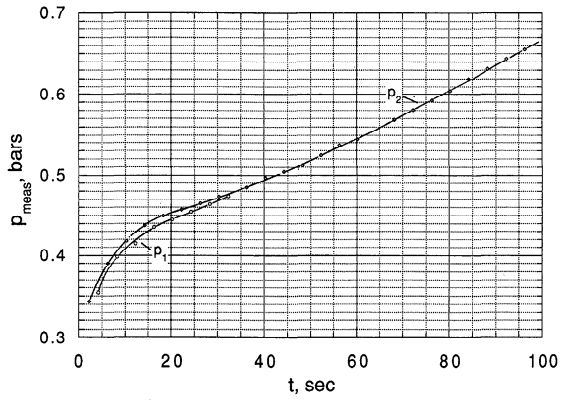

Figure 8. Expanded graph of the first 100 s of pressure data.

B) was −7 mbar at 20 s and −12 mbar at 40 s, while those for p_1 were ~1/8 as large.

Sensor internal temperatures were measured every 64 s to permit corrections for the expected small changes in calibration with temperature. But sensor temperatures dropped from −1.5° to −50°C (the temperature of the outside atmosphere) in the first 10 min of descent. From this minimum, temperatures increased to +118°C at the end of the mission, lagging behind the temperature of the atmosphere by only ~34°C. The specified operating temperature range of −20° to +50°C was thus grossly exceeded. Sensor temperatures were outside the range of preflight calibrations at pressures between 1.5 and 6 bars and above 12 bars. Extrapolation of the calibrations to cover the temperature range experienced is described in Appendix B.

As noted, sensor temperature rates were also an important consideration. They varied from −7.3 to +4.5°C/min, well outside the specified limit of 1°C/min. This prevented the sensors from attaining thermal equilibrium and made temperature rate corrections necessary. Fortunately, we had tested flight sensors for the effect on zero readings of temperature rates from −1° to +2.9°C/min in 1984 and 1985. At pressures above 4 bars in Jupiter descent, the p_3 sensor warming rate was from 3° to 4.5°C/min, requiring only moderate extrapolation of the preflight test results. The 7.5°C/min cooling early in the descent, however, greatly exceeded the preflight test range. We therefore tested the flight spare and engineering unit sensors in 1996 at high cooling rates to characterize their behavior when exposed to simulated flight temperature histories. To account for differences among the sensors, test results were scaled to apply to the flight sensors (Appendix B). This gave us a reasonably confident basis for temperature rate corrections. The corrected and uncorrected data are compared in Figure 9 for the 4 and 28 bar ranges. The p_2 corrections are largest near 1.6 bars; p_3, near 2 bars. Estimated uncertainties are given in Table 4. Estimated pressure uncertainty did not exceed 2% for the more sensitive on-line sensor. Figure 10 compares the corrected p_2 and p_3 data at $p < 4$ bars, where p_3 uncertainty becomes appreciable. The maximum disagreement, ~0.1 bar at 1.7 bars, is consistent with the root-sum-square (rss) combined uncertainties at this pressure level.

Starting at ~2600 s (p = 14 bars, electronics temperature 54°C), four high readings occurred at the same time in each major frame of pressure data (Figure 7). The high-point deviations grew larger with time. They were found to coincide with the application of voltage to one of the engineering temperature sensors, disappearing when the voltage source was switched off. We concluded that the anomalous readings were caused by a multiplexer current leak between the voltage source and the signal lines. The 28 readings in each major frame taken when the voltage source was off are a smooth continuation of the variation before 2500 s and are considered valid data.

The pressure sensor internal electronics and the A/D converter were calibrated in descent once/major frame (every 64 s), by applying an accurate 1.250 V signal to the sensor test leads. This produced an incremental signal, ideally 256 counts, to the pressure reading. Through all but one sample in 2750 s of descent to a pressure of 15 bars, the test signals read this ideal value within 1 count (Figure 11), confirming that the pressure sensor electronics were accurate within 0.4%. Coincident with the onset of spikes in the pressure data, the calibration signals decreased to a final value of 213 counts at p = 21.3 bars. Pressure sensor degradation is not required to explain this anomaly. The current leak in the multiplexer switch, which caused the pressure spikes, could also impose a drain on the calibration voltage supply and explain the drop-off in calibration signal. Correcting the measured pressures by the ratio of the normal calibrate signal to its observed value produced upward curvature in $p(t)$ and unrealistically high pressures, up to 26.4 bars at the end of the mission. From this, we conclude that the calibration signal was faulty. Additional checks of the central instrument electronics were performed in each major frame, and found normal. We believe the sensor data between anomalies were valid to mission's end.

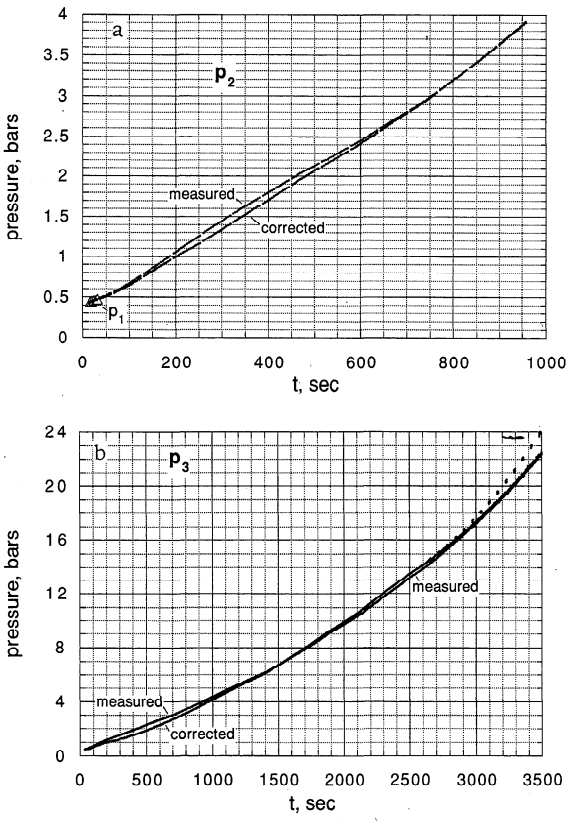

Figure 9. Comparison of (a) low- and mid-range and (b) high-range pressure data corrected for sensor temperature rate with uncorrected data of Figure 7.

Table 4. Order of Uncertainties in Pressure Data

p, bars	T_p, °C	dT_p/dt, C/m	δp_2, b	δp_3, b
		Scale Factor and Resolution		
0.5	−0.5	−2.1	0.004	0.028
1	−8.1	−6.2	0.004	0.028
2	−33.0	−3.9	0.004	0.028
3	−42.2	−0.75	0.004	0.028
4	−40.6	+1.5	0.004	0.028
6	−22.1	3.6		0.028
10	+22.8	4.2		0.028
15	72.0	3.9		0.028
20	105.4	3.0		0.028
		Offset Extrapolation		
0.5	−0.5	−2.1	0	0
1	−8.1	−6.2	0	0
2	−33.0	−3.9	0.006	0.087
3	−42.2	−0.75	0.046	0.123
4	−40.6	+1.5	0.038	0.117
6	−22.1	3.6		0
10	+22.8	4.2		0
15	72.0	3.9		0.073
20	105.4	3.0		0.203
		Temperature Rate Correction		
0.5	−0.5	−2.1	0.009	0.022
1	−8.1	−6.2	0.018	0.066
2	−33.0	−3.9	0.011	0.041
3	−42.2	−0.75	0.002	0.008
4	−40.6	+1.5	0.003	0.016
6	−22.1	3.6		0.038
10	+22.8	4.2		0.045
15	72.0	3.9		0.041
20	105.4	3.0		0.032
		Combined Uncertainty, Root-Sum-Square		
0.5	−0.5	−2.1	0.010	0.036
1	−8.1	−6.2	0.018	0.072
2	−33.0	−3.9	0.013	0.100
3	−42.2	−0.75	0.046	0.126
4	−40.6	+1.5	0.038	0.121
6	−22.1	3.6		0.047
10	+22.8	4.2		0.053
15	72.0	3.9		0.088
20	105.4	3.0		0.207

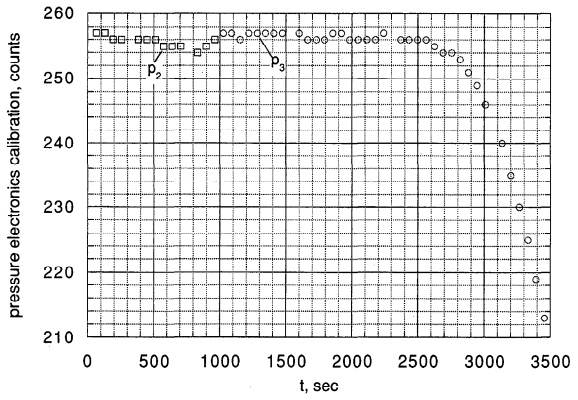

Figure 11. Pressure sensor calibration data taken every 64 s in descent. The normal reading from preflight tests and in cruise was 256 counts.

3.3. Accelerations

The axial accelerometer data from z_1 and z_2 sensors in the entry period are shown in Figure 12 (z_2 readings are reduced by a factor of 3 to separate them from z_1 and permit detailed comparison). It is evident that the two sensor channels agree very closely. The first reading retained in memory was 21 μg_E (Earth microgravities). The sensors advanced through four ranges (where indicated). Range junctures were smooth, but the first sample after range change was typically lost because of ranging transients. The maximum deceleration, 228 g_E, occurred 108 s before the start of descent mode. After $t = -50$ s, the probe was in subsonic descent, with small net deceleration. Throughout the acceleration profile, small irregularities in slope and curvature can be seen on close examination. These are the source of oscillations in the density and temperature profiles which we will present.

An unexpected, highly regular oscillation of 7 μg amplitude at the roll period, ~6 s, was recorded near the sensor threshold. Rolling motion about the z axis should not introduce z axial accelerations unless there is significant sensor misalignment, but the sensors were aligned to the probe axes within ~0.001 radian. This signal possibly resulted from complex dy-

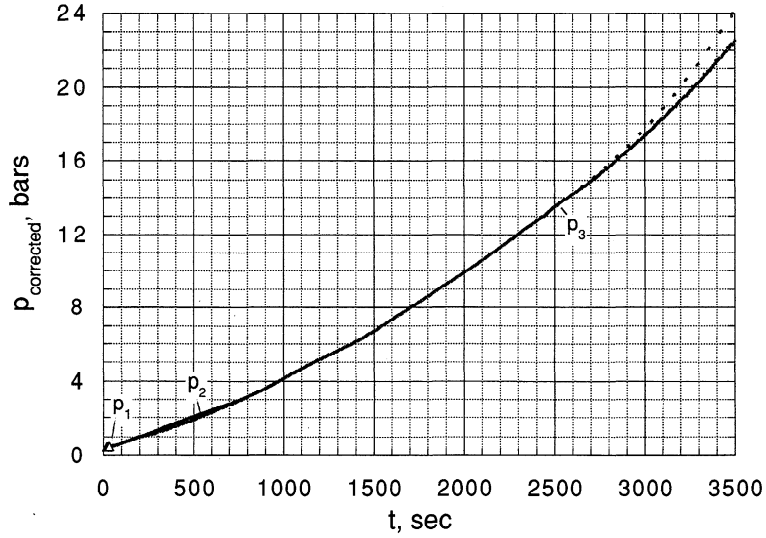

Figure 10. Comparison of corrected pressure data from the 4- and 28-bar range sensors.

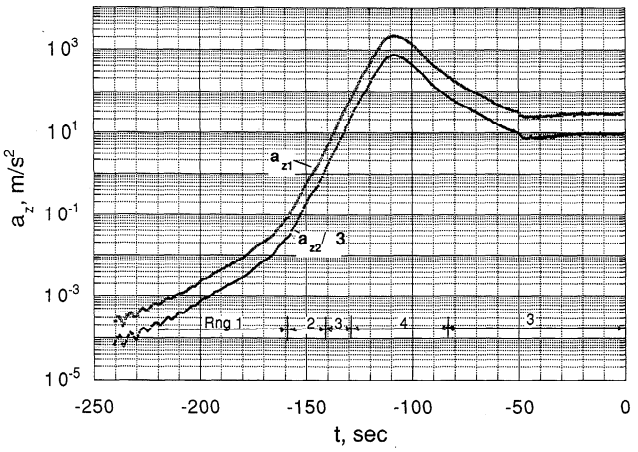

Figure 12. Comparison of axial accelerations of the probe from two sensors during hypervelocity entry. The data extend over a dynamic range of 2×10^7. Four sensor ranges were used, as shown. The z_2 sensor data have been divided by 3 to separate the two sets and expedite comparison. Descent mode starts at $t = 0$, which preceded parachute deployment by ~5 s.

namics associated with mass asymmetry, such that the roll axis was inclined to the z axis. We also considered the possibility that emf's were induced by conductors cutting the magnetic field of Jupiter at the high velocity of entry, the sign reversing with each half cycle of roll. In any case, the fact that this oscillation is synchronous with the rolling motion indicates that it does not reflect probe deceleration. It was therefore smoothed out of the data. As acceleration increased, the 7.5 μg oscillation became a negligible perturbation.

At $t = -50$ s there was a nearly discontinuous slope change in $a_z(t)$ (see the enlarged portion of the z_1 record (Figure 13)). This is a signature of passing through $M = 1$ seen previously in the Planetary Atmosphere Experiment Test (PAET) Earth-atmosphere probe data [*Seiff et al.*, 1973]. Subsequently, the data scatter increases as a result of unsteadiness of the subsonic wake, which causes unsteadiness in the drag coefficient, a well-known characteristic of subsonic aerodynamics of blunt

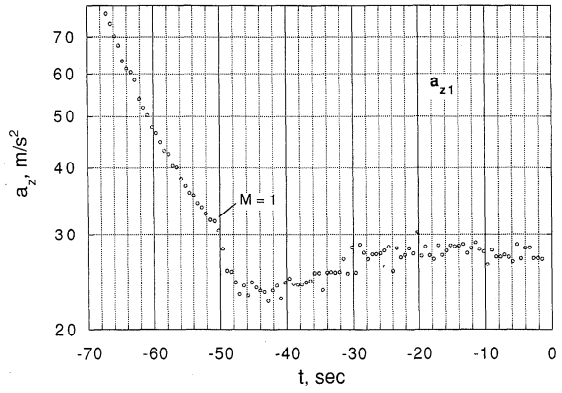

Figure 13. Expanded a_{z1} data at the time the probe passed through a Mach number of 1. This occurred at $t \sim -50$ s, when the probe was at an altitude of 50.6 km, $p = 4.6$ mbar. Subsequently, in subsonic descent, the accelerations were more irregular, as a result of aerodynamic buffeting created by unsteady wake flow.

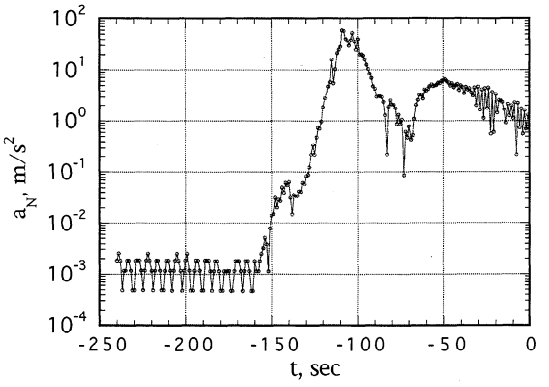

Figure 14. Accelerations normal to the probe z axis. These are the resultant of the x and y axis accelerations. Prior to −150 s, the readings were below the sensor threshold. The oscillating signal in the early data is synchronous with the probe roll rate and is not aerodynamically induced (see text).

bodies, including baseballs. It increases the scatter in the density profiles below ~50 km altitude.

Normal accelerations during entry are shown in Figure 14. At entry and until −160 s, they were below sensor thresholds. During this time, the signal was oscillating with an amplitude of 0.0007 m/s^2 (70 μg) and, again, a 6 s period. This is 10× the amplitude seen in the z axis and suggests that the source was dynamic rather than electromagnetic. After coming above threshold, a_N peaked at $8g_E$, simultaneously with a_z at −108 s. These amplitudes correspond to an angle of attack of 2.2° at −110 to −95 s during peak deceleration and massive ablation. The initial angle of attack, inferred by reconstructing the oscillation upward, is ~5.7° at the start of the data. Below $Ma = 2$, dynamic instability led to growth of the angle of attack to a peak of ~14° at $Ma = 1$. Subsequently, as the probe decelerated to $Ma \sim 0.5$, angle of attack decreased approximately linearly with time to ~2° at the start of descent mode. These features can be seen in the a_N data (Figure 14).

Shortly after the start of descent, the parachute opened. Although the deceleration pulse could not be reconstructed in detail with 16 s time resolution of accelerations, the velocity change recorded in the first 50 s of descent was 348 m/s, mostly occurring in the first 16 s. Added to the velocity determined from the pressure data at $t = 50$ s (90 m/s), this gave the velocity at the start of descent, 438 m/s. After the first 250 s, measured accelerations (Figure 15) were within 0.1 m/s^2 of the acceleration of gravity on Jupiter, g_j, and after 500 s, measured values were less than g_j. This was a result of the prograde winds carrying the probe, leading to increased centrifugal acceleration. The horizontal wind variation with depth derived from these data substantially agreed with Doppler tracking inferences [*Seiff et al.*, 1997b].

The accelerations normal to the probe axis in parachute descent (Figure 16) were nearly constant with time before and after a large pulse which occurs during the time the sensor temperatures are below −20°C [*Seiff et al.*, 1996a]. Because the x axis sensor did not operate properly in the manufacturer's tests at $T < -15$°C, data taken at < −15°C were not expected to be valid. (At this temperature, the bellows provided to compensate for thermal contraction of the fluid in the sensor reached the end of its travel. With further cooling, a vapor pocket formed, causing a large offset change.)

In the period of valid data, the constant $a_N = 0.9$ m/s^2 peak

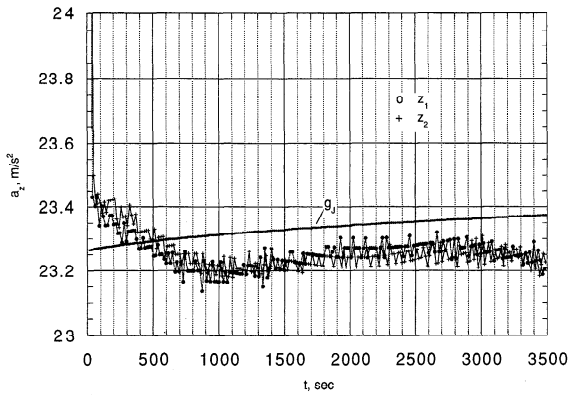

Figure 15. Axial accclerations of the probe in parachute descent, as a function of pressure. The z_1 and z_2 sensor data agree within about ± 0.05 m/s^2. The sampling interval was 16 s. Each sample is the average of 512 readings. The deviations from g_j are associated with real deceleration of the probe, visible in the first 500 s, and with centrifugal accelerations due to the probe's being carried along at the velocity of the winds [*Seiff et al.*, 1997b].

amplitude has been interpreted as a measure of swinging motion of the probe hanging from the parachute [*Seiff et al.*, 1996a]. The amplitude is 2.2°, remarkably small, considering the potential for disturbance from turbulence in the atmosphere. The minimum amplitude indicated by $(a_N)_{\min}$ is 0.6°. There is an interesting peak in $(a_N)_{\max}$ defined by three consecutive samples at 3000 s. This occurs at a pressure of 16 bars, where data, shown below, indicate a change in atmospheric stability.

Some of the turbulence data from the z_1 accelerometer in descent are shown in Figure 17. At eight levels, ± 0.059, ± 0.118, ± 0.236, and ± 0.472 g (g refers to Earth g), the number of positive going excursions of the acceleration were counted in a 96 s sampling interval. The data shown are for ± 0.059 g. These channels recorded typically 250 counts in 96 s, or 2.5/s. At 40 m/s descent velocity, the vertical scale is 16 m. The next levels, ± 0.118 g, were asymmetric, the negative channel counting typically 55 ± 12, events and the positive 20 ± 14.

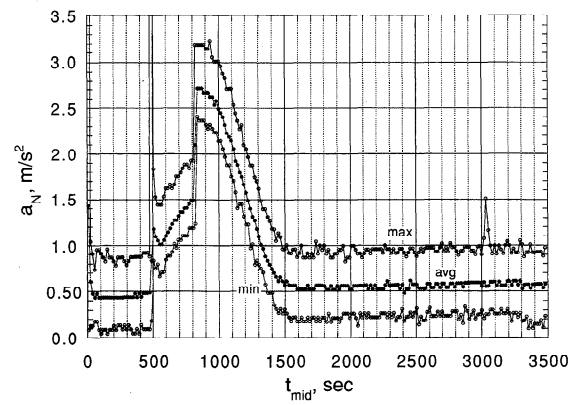

Figure 16. Accelerations normal to the z axis in parachute descent. Maximum, mean, and minimum accelerations over 16 s intervals were transmitted. The maximum in the first 500 s and after 1500 s was ~0.9 m/s^2. The intervening excursion to a peak of 3.2 m/s^2 resulted from an a_x sensor malfunction at temperatures below −20°C.

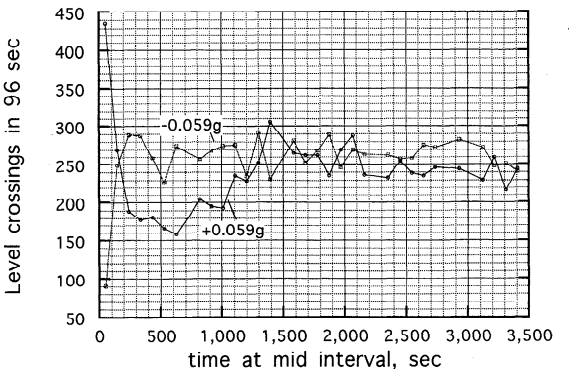

Figure 17. Axial turbulence counts in the channel counting the lowest level perturbations. In the first sample the high count level was influenced by parachute-opening dynamics.

The data were also much less uniform than at the lower levels. Levels 3 and 4 were empty, zero counts, except for an occasional 1 or 2 counts crossing -0.236 g.

The normal acceleration counting levels were 0.004, 0.012, 0.024, and 0.048 g. The lowest counting level was empty in all samples, and the second had only a few counts (4–11) early in the descent because angles of attack never permitted a_N to go below these levels (Figure 16). The third level had ~50 crossings/sample in the first 500 s, was empty from 500 to 1500 s (the reason is evident from Figure 16), and 2–10 crossings/sample in the last 2000 s. The 0.048 g level was crossed ~70 times/96 s early and ~50 times/96 s for the last 2000 s.

4. Analysis of Data

4.1. Lower Atmosphere

Altitudes and descent velocities in the lower atmosphere were defined as functions of time from measured pressures and temperatures. Assuming hydrostatic equilibrium,

$$dp = -\rho g\, dz = -(pg/RT)\, dz \qquad (1)$$

Probe altitudes were calculated by integrating (1) using measured pressures and temperatures. Probe descent velocities were calculated by writing the differentials in (1) as time derivatives:

$$w_p = dz/dt = -(RT/pg)(dp/dt) \qquad (2)$$

To minimize digital resolution uncertainty, the rate of increase of pressure was determined from a marching 15-point quadratic fit to $p(t)$, with dp/dt determined analytically at the central point. The descent interval covered by 15 points is 56 s and corresponds to an altitude interval of 2.2 km at 40 m/s descent velocity. Descent velocities were also calculated using 7- and 9-point quadratic smoothing and 15-point cubic smoothing of $p(t)$ for comparison. As will be shown, all smoothing approaches yielded fluctuating descent velocities. We will discuss the atmospheric turbulence implications of the descent velocity fluctuations.

Pressures as a function of time provided to other probe investigators for depth reference were based on the dry adiabatic atmosphere which was a close fit to the temperature-pressure data (see below). The timescale for the adiabat was taken from the very accurate temperature data. The descent velocities used as a key input to the Doppler determination of

deep atmosphere winds also were derived for the dry adiabatic atmosphere.

Atmospheric density was calculated from the equation of state. Gas composition and gas constant were allowed to vary with pressure level, consistent with the measured He/H_2 ratio, 0.136/0.864 = 0.1574 [*von Zahn et al.*, this issue], the minor constituent variations measured by the neutral mass spectrometer [*Niemann et al.*, this issue], and NH_3 abundance profile determined by radio science [*Folkner et al.*, this issue] and the probe net flux radiometer [*Sromovsky et al.*, this issue]. Minor species number density ratios to H_2 selected were as follows: for H_2O, $\sim 10^{-6}$ at 0.4–5 bars, 5.6×10^{-5} at 5–10 bars, and 0.00056 at >10 bars, and for CH_4, 0.0021. For NH_3, ratios chosen were 3×10^{-6} at $p < 2$ bars, 2.24×10^{-4} (solar) at 2–5 bars [*Sromovsky et al.*, this issue], 4.48×10^{-4} at 5–10 bars, and 6.72×10^{-4} at >10 bars [*Folkner et al.*, this issue]. The resulting mean molecular weight μ varied smoothly from 2.3105 amu at 0.4 bar to 2.3323 amu at 22 bars and was represented by

$$\mu = 2.3104 + 0.0003722p + 2.8403 \times 10^{-5} p^2 \quad (3)$$

where p is in bars. The gas constant varied from 3598.5 to 3564.8 J/kg K. This variation affects density by ~1% and has small effect on altitude and descent velocity. Compressibility factors Z, in $p = Z\rho RT$, were taken from the National Bureau of Standards (NBS) tables of *Hilsenrath et al.* [1960] for pure hydrogen. They ranged from 1.000 at 0.4 bars to 1.011 at 22 bars and were represented by a cubic polynomial in p.

Lapse rates, dT/dz, were calculated from curve fits to the ln T versus ln p data, and the hydrostatic, perfect-gas relation:

$$dT/dz = -(g/R)(d \ln T/d \ln p) \quad (4)$$

Equivalently, the derivative dT/dz in the descent profile gave identical results.

4.2. Upper Atmosphere

Atmospheric densities ρ were derived from the measured accelerations by use of Newton's second law of motion and knowledge of the probe aerodynamics,

$$\rho = 2(m/C_D A)(a_z/V_r^2), \quad (5)$$

where the drag force is $C_D(1/2)\rho V_r^2 A$; m, C_D, and A are the probe mass, drag coefficient, and frontal area; a_z is the probe deceleration; and V_r is the probe velocity relative to the atmosphere. V_r for use in (5) and altitude z, the independent variable, were determined as functions of time by reconstructing the probe trajectory from measured accelerations and initial conditions. Pressures were then determined by integrating (1) with the measured $\rho(z)$. The initial value of pressure at the first datum is undetermined and must be assumed. We do this by choosing initial temperatures T_i over a plausible range, calculating p_i, and deriving the structure for each choice. Results are presented below for a range of T_i. The solutions converge within one decade of pressure increase. From the densities and pressures, atmospheric temperatures $T(z)$ are calculated from the equation of state $T = p\mu/\rho R_u$ using a model to represent the upper atmosphere composition (see below), where μ is a function of altitude and R_u is the universal gas constant.

The trajectory was reconstructed by integrating measured accelerations and a model of the acceleration of gravity in the equations of motion to define the departure from the initial state at entry. Four parameters, V_r, γ, z, and λ fully define the trajectory, where γ is the flight path angle below horizontal and λ is heading angle measured clockwise from east.

The trajectory was reconstructed following the procedure of the late *D. R. Chapman* [1958], except that Chapman solved the equations of motion approximately, while we numerically integrate the complete equations. In the coordinate system used, x is the zonal coordinate, horizontal and positive eastward; y is the meridional coordinate, positive northward; and z is vertical. The differential equations solved were

$$\begin{aligned} dV_x/dt &= -a_z(\cos \gamma_r)(\cos \lambda_r) - V_x V_z/(R_0 + z) \\ dV_y/dt &= -a_z(\cos \gamma_r)(\sin \lambda_r) - V_y V_z/(R_0 + z) \\ dV_z/dt &= -a_z(\sin \gamma_r) + V_x^2/(R_0 + z) - g_u \end{aligned} \quad (6)$$

with initial conditions

$$\begin{aligned} V_{x0} &= V_{r0}(\cos \gamma_r)(\cos \lambda_r) + V_a \\ V_{y0} &= V_{r0}(\cos \gamma_r)(\sin \lambda_r) \\ V_{z0} &= V_{r0}(\sin \gamma_r) \end{aligned}$$

where a_z is measured probe z axis acceleration, $V_a = (R_0 + z)\Omega \cos \theta$, $V_r = [(V_x - V_a)^2 + V_y^2 + V_z^2]^{1/2}$, R_0 is planet radius at 1 bar level (71,334 km), γ_r is relative flight path angle below horizontal, λ_r is relative heading angle, clockwise from east, θ is planetocentric latitude, and Ω is planet spin rate, 1.7585323×10^{-4} radian/s. After each integration step, the coordinates were rotated about y so that for every time, z is vertical. Note that g in (1), (2), and (4) is corrected for centrifugal acceleration resulting from planet rotational velocity Ω, whereas g_u in (6) is the gravitational acceleration uncorrected for centrifugal acceleration. This correction is represented by the term $V_x^2/(R_0 + z)$ in the third differential equation.

The effect of angle of attack α on the trajectory is minimal because α is oscillatory. As a result, forces across the flight path produce a small oscillatory or swerving motion about a mean flight path which is essentially unaltered from that for zero angle of attack. Angle of attack effects could therefore be neglected in reconstructing the trajectory.

In (5), C_D and a_z are weak functions of α in the small-angle range up to ~15°, and their variations with α cancel. In (6), α is assumed to be zero, so that force along the probe axis is identical to force along the flight path. In free molecular flow, for which $C_z \sim C_D \cos \alpha$, at the initial angle, ~5.7°, C_z differs from C_D by 0.5%. Near peak deceleration, where α was ~2°, test data show C_z essentially identical to C_D. Transonically, when α grew to ~14°, some opportunity for difference between C_z and C_D exists but was unaccounted for.

The differential equations were solved by use of an Adams-Moulton fixed-step-size procedure. A number of complications, discussed in the following paragraphs, were encountered in performing the solutions.

The oscillatory component of the signal at the start of data was about 70 $\mu m/s^2$, about 28% as large as the mean deceleration (Figure 12). This input, discussed above, was removed by fitting a sinusoid to the data and subtracting it from the measured values to obtain aerodynamic decelerations. Another editing task was to remove the spurious readings on range change. Typically, this required discarding the first point on each new range.

The initial values of V_r, γ_r, λ_r, and longitude were determined by the Galileo Project navigation team with high accu-

Table 5. Upper Atmosphere Composition Model

z, km	T, K	p, μbar	D_{He}, cm^2/s	f_{He}	f_{CH_4}	f_H	f_{H_2}	μ, amu
1001	880.1	0.001117	9.26e+09	0.0007565	1.969e−18	0.01648	0.9828	2.001
900.6	863.5	0.002110	4.75e+09	0.001426	1.687e−16	0.01201	0.9866	2.007
798.3	873.6	0.003996	2.56e+09	0.002685	1.440e−14	0.008741	0.9886	2.013
699.6	743.2	0.007776	9.91e+08	0.005165	1.437e−12	0.006271	0.9886	2.020
600.0	671.0	0.01736	3.71e+08	0.01122	3.355e−10	0.004200	0.9846	2.034
500.0	548.2	0.04222	1.07e+08	0.02569	1.083e−07	0.002696	0.9716	2.064
400.3	378.4	0.1438	1.65e+07	0.06846	6.699e−05	0.001507	0.9300	2.151
350.3	208.5	0.4309	1.93e+06	0.1092	0.0007543	0.001062	0.8890	2.242
301.6	198.1	2.022	3.76e+05	0.1302	0.001558	0.0008981	0.8673	2.296
201.0	157.4	1.177e+02	4.31e+03	0.1352	0.001806	0.0008626	0.8621	2.309
101.1	156.8	6.703e+03	7.52e+01	0.1353	0.001810	0.0008620	0.8620	2.309
22.67	120.9	3.626e+05	1.090	0.1353	0.001810	0.0008620	0.8620	2.309

Read 9.26e+09 as 9.26×10^9.

racy, and were provided to us by Jon Neff. The values supplied for a probe altitude of 450 km above the 1 bar level are given in Table 1. Time at 450 km could not be well determined by the navigation team. We determined this time by adjusting it to give the correct altitude (above the 1 bar level) at $t = 0$, as determined by the instrument at the start of the parachute descent. The value of time at 450 km so determined was −166.14 s, more than 30 s different from the navigation team estimate (slightly greater than their 1-sigma uncertainty, 26 s). The differential equations were integrated upward from 450 km to determine trajectory parameters up to the level of first data, which was 1029.2 km.

Initial values of velocity, altitude, pressure, and temperature measured in parachute descent provided a valuable constraint on final values derived in the analysis of the entry data. Adjustments were made to the time at 450 km, to the accelerometer scale factors on range 4 (wherein the largest velocity loss occurred), and to the total mass loss (within its uncertainty range) to achieve a close match to conditions at the start of descent. The altitude at the start of descent was 23.02 km above the 1 bar level, and velocity was 438 m/s. The optimum velocity match was obtained for a correction factor on an accelerometer scale factor of 1.000031, well within the accuracy with which it was determined in calibration. The mass loss model has small but discernible effects on the velocities and densities during entry after $t = -120$ s, i.e., at altitudes below 150 km (Figure 3, Table 6). Continuity in the density profile across mode change, to be shown, pointed to a final probe mass of 241.33 kg, which gave the best match of all considered parameters.

The determination of the atmospheric density in the vicinity of $Ma = 1$ required careful treatment, since drag coefficient decreases by 30% in going from $Ma = 1.1$ to 0.9. The precise time at $Ma = 1$ is thus locally important. Furthermore, Ma depends on the speed of sound, which in turn, depends on c_p/c_v, a function of temperature. We tried several approaches to this problem but never achieved a completely smooth density variation through $Ma = 1$, the best result being approximately ±5% about a smooth variation. This problem is restricted to approximately ±7 s about the time of $Ma = 1$, before and after which density determination is normal.

The entry trajectory terminates near the cloud tops, where there are known zonal winds ~100 m/s [*Atkinson et al.*, this issue]. We examined the effect of including winds in this portion of the trajectory, where their velocities are ~1/5 × descent velocity and therefore affect resultant velocity by ~2%. The problem is complicated by the fact that the probe will acquire the velocity of the wind with a response time, $V/g \sim 20$ s. When the wind velocity is acquired, the probe effectively descends vertically in a reference frame moving with the wind. Although a number of trials were made at incorporating winds into the reconstruction, they were handicapped by lack of knowledge of the winds at these levels and did not significantly affect the atmosphere profiles obtained. The results presented herein are for the case of zero wind velocity.

4.3. Upper Atmosphere Composition Model

The upper atmospheric composition determines the mean molecular weight μ used in the equation of state to calculate upper atmosphere temperatures. As shown in Table 5, μ varies from 2.309 near the tropopause (which is above the clouds) to 2.001 at 1.001 nbar, where composition approaches pure molecular hydrogen.

The composition model was calculated by iteratively solving the hydrostatic equation and the equation of molecular diffusion. Given the density profile $\rho(z)$ measured by the decelerating spacecraft, we make an initial estimate of the temperature T_i at the highest altitude, from which a first approximation pressure at z_i, $p_i = \rho R_u T_i/\mu_{zi}$ is calculated. In the initial approximation, the mixing ratios and hence $\mu(z)$ are assumed constant with height. The mixing ratios at the tropopause are taken to be $n_{He}/n_{H_2} = 0.157$ [*von Zahn et al.*, this issue], $n_{CH_4}/n_{H_2} = 0.0021$ [*Niemann et al.*, 1996], and $n_H/n_{H_2} = 0.001$. NH_3 and H_2O are assumed to be fully condensed and removed in the cold traps provided by the ammonia and water clouds. Since the model does not include photochemistry, the H fraction was artificially introduced to give approximately the correct H/H_2 ratio in the exosphere [*Gladstone et al.*, 1996]. This does not significantly influence the molecular weight profile. The tropopause molecular weight is then

$$\mu = f_{H_2}(\mu_{H_2}) + f_{He}(\mu_{He}) + f_H(\mu_H) + f_{CH_4}(\mu_{CH_4}) = 2.3093 \quad (7)$$

differing slightly from the lower atmosphere model because the traces of water and ammonia have been frozen out above any existing clouds. Here, $f_{H_2} = 1 - (f_{He} + f_{CH_4} + f_H)$, and f_{He}, for example, is the helium molar mixing ratio with respect to the total atmosphere. With the initial pressure specified, the pressure and temperature variations with altitude, $p(z)$ and $T(z)$, are found by integrating the equation of hydrostatic

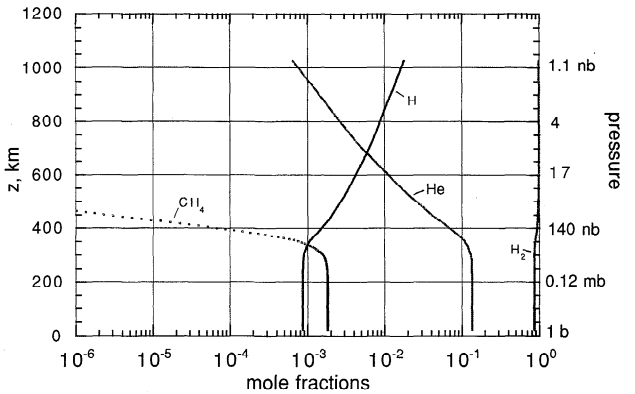

Figure 18. Upper atmosphere composition model. Molecular hydrogen is the dominant constituent (0.98 mole fraction) at 1000 km, where atomic H replaces He as second most abundant (0.02 mole fraction).

equilibrium, as described above. The scale heights H, number densities n, and diffusion coefficients D are then calculated for each altitude. The diffusion coefficients have the form

$$D = aT^s/n \tag{8}$$

where the coefficients a and s are species dependent. The minor species are considered to diffuse through H_2. For He, $a = 5.27 \times 10^{17}$ and $s = 0.75$. For CH_4, $a = 2.298 \times 10^{17}$ and $s = 0.765$, and for H, $a = 2.296 \times 10^{17}$ and $s = 0.728$ [*Mason and Marrero*, 1970].

If the escape rate is ignored, the (typical) diffusion equation of He is given by the equation of vertical flux [*Gladstone et al.*, 1996]:

$$df_{He}/dz = -f_{He}D/(D + K)(1/H)[(\mu_{He}/\mu) - 1] \tag{9}$$

The eddy diffusion coefficient K is assumed to be a constant 5×10^6 cm^2/s [*Yelle et al.*, 1996]. These equations are integrated for each species upward from the tropopause to define the fractional abundances of He, CH_4, and H as functions of altitude. The molecular weight profile is calculated, and another iteration follows. This continues to convergence.

The upper atmospheric composition model derived is summarized in Table 5 and shown in Figure 18. The variation of mean molecular weight with altitude is shown in Figure 19. The table includes the diffusion coefficients for helium. The onset of change in mean molecular weight is at 250 km, but rapid changes in composition begin between 300 and 350 km, which can be designated as the homopause region.

5. Probe Trajectory

5.1. Entry Trajectory

Table 6 lists the parameters of the reconstructed entry trajectory versus time in the 240 s data collection period. The first group of parameters, the altitude, velocity, and flight path angle define the trajectory. (The heading angle never deviated significantly from 2° clockwise from east.) In the next two columns, probe mass and diameter are constant at their initial values down to 180 km, then change rapidly between 150 and 75 km, which is the interval of rapid ablation. The last four columns list the aerodynamic parameters, Ma, Re, Kn, and the drag coefficients employed in the analysis.

Velocity relative to the rotating, wind-free atmosphere, shown in Figure 20, was near 47 km/s during the first 115 s as the probe traversed the tenuous atmosphere above 215 km. In the following 60 s, the major velocity loss occurred as the probe descended to 55 km altitude and decelerated to ~1 km/s. The flight path angle relative to the rotating atmosphere (Figure 21) remained shallow through the high-speed period, from ~10° at 1029 km to ~7° at an altitude of 80 km. At this point, the flight path turned rapidly toward vertical, reaching 83° at $t = 0$. The parachute was deployed 14 s later.

5.2. Descent Profile

The descent trajectory is summarized in Table 7, which gives both the state variables and the trajectory parameters based on the dry adiabat which best fit the temperature-pressure data (see below). Deviations of the data from this adiabat were comparable to uncertainties in the data at $p < 15$ bars. The descent velocities and lapse rates determined from measured pressures and temperatures will be presented and discussed below.

Altitudes shown as a function of time in Figure 22 were derived from (1) for this adiabat. The altitude of first meaningful descent mode data was ~18.5 km above the 1 bar level, just above the first entry in Table 7. Data communication was maintained to a depth >130 km below the 1 bar level. The pressure-depth relationship is shown in Figure 23. The variation of temperature with depth is nearly linear (Figure 24) because the temperature lapse rate is nearly constant. Probe descent velocities derived from the dry adiabat by use of (2) are shown as a function of pressure in Figure 25. Times needed to define dp/dt were interpolated from the very accurate temperature data at 1 K steps, and dp/dt was determined by fitting quadratics to the pressure data over marching, 7-point intervals. Velocities ~90 m/s at 0.6 bar decreased with increasing atmospheric density to ~26 m/s at end of mission. Figure 25 indicates a fluctuating descent velocity with ~0.5–2 m/s amplitude throughout the descent. There are features with ~3 m/s amplitude indicated at 0.8 and 1 bar, and a dip of ~7 m/s centered at 1.4 bars, which is near the nephelometer cloud bottom [*Ragent et al.*, this issue]. The fluctuations are not attributable to noisy data, since the input "data" were from an exact adiabat. These results will be further discussed in the section below, Winds and Turbulence.

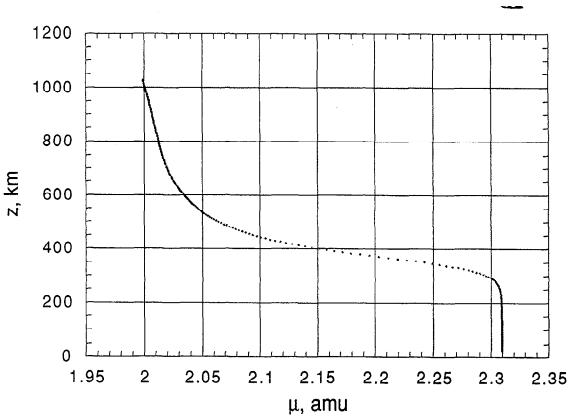

Figure 19. Mean molecular weight model used to calculate atmospheric temperatures.

Table 6. Entry Trajectory

t, s	z, km	V, km/s	γ, deg	m, kg	d, m	M	Re	Kn	C_D
−240.0	1027.1	47.130	−10.61	338.93	1.265	20.58	0.0692	443.	2.060
−235.0	983.96	47.151	−10.46	338.93	1.265	20.77	0.0924	335.	2.060
−230.0	941.44	47.171	−10.31	338.93	1.265	21.03	0.125	250.	2.060
−225.0	899.49	47.191	−10.16	338.93	1.265	21.02	0.163	192.	2.060
−220.0	858.13	47.211	−10.02	338.93	1.265	20.89	0.206	151.	2.060
−215.0	817.36	47.230	−9.87	338.93	1.265	20.88	0.265	118.	2.060
−210.0	777.17	47.249	−9.72	338.93	1.265	21.19	0.358	88.3	2.058
−205.0	737.57	47.268	−9.57	338.93	1.265	21.87	0.515	63.2	2.054
−200.0	698.56	47.287	−9.42	338.93	1.265	22.90	0.793	43.0	2.051
−195.0	660.15	47.305	−9.27	338.93	1.265	23.69	1.19	29.6	2.047
−190.0	622.32	47.323	−9.12	338.93	1.265	24.04	1.70	21.1	2.045
−185.0	585.09	47.341	−8.97	338.93	1.265	24.17	2.35	15.3	2.043
−180.0	548.45	47.358	−8.82	338.93	1.265	24.51	3.35	10.9	2.040
−175.0	512.41	47.376	−8.68	338.93	1.265	26.27	5.81	6.74	2.026
−170.0	476.96	47.393	−8.53	338.93	1.265	27.27	9.43	4.31	2.010
−165.0	442.11	47.409	−8.38	338.93	1.265	28.48	15.90	2.67	1.991
−160.0	407.87	47.425	−8.23	338.93	1.265	32.93	40.70	1.21	1.953
−155.0	374.22	47.441	−8.08	338.93	1.265	38.89	1.30e+02	0.446	1.875
−150.0	341.18	47.455	−7.93	338.93	1.265	45.77	5.46e+02	0.125	1.726
−145.0	308.74	47.466	−7.78	338.93	1.265	45.07	1.47e+03	0.0453	1.526
−140.0	276.91	47.468	−7.63	338.93	1.265	51.81	7.85e+03	0.00981	1.153
−135.0	245.70	47.437	−7.48	338.93	1.265	51.33	2.76e+04	0.00278	1.087
−130.0	215.15	47.300	−7.33	338.87	1.265	51.26	9.60e+04	0.000798	1.049
−125.0	185.39	46.822	−7.18	338.51	1.265	50.78	3.17e+05	0.000238	1.030
−120.0	156.76	45.377	−7.04	336.39	1.264	47.68	8.55e+05	8.31e−05	1.026
−115.0	130.16	41.495	−6.92	324.53	1.261	45.00	2.55e+06	2.65e−05	1.019
−110.0	107.67	32.770	−6.85	287.72	1.246	36.10	5.43e+06	9.98e−06	1.009
−105.0	91.391	21.965	−6.89	254.15	1.223	23.69	6.62e+06	5.33e−06	1.004
−100.0	80.749	13.669	−7.10	244.19	1.213	15.33	7.45e+06	3.07e−06	1.001
−95.0	73.873	8.444	−7.58	242.09	1.211	9.91	7.53e+06	1.96e−06	1.010
−90.0	69.146	5.535	−8.43	241.39	1.210	6.49	6.20e+06	1.56e−06	1.033
−85.0	65.533	3.828	−9.75	241.34	1.210	4.60	5.64e+06	1.22e−06	1.066
−80.0	62.535	2.767	−11.67	241.33	1.209	3.31	4.59e+06	1.08e−06	1.146
−75.0	59.878	2.051	−14.30	241.33	1.207	2.50	4.07e+06	9.12e−07	1.254
−70.0	57.438	1.543	−17.80	241.33	1.207	1.93	3.92e+06	7.35e−07	1.345
−65.0	55.135	1.188	−22.35	241.33	1.207	1.50	3.58e+06	6.25e−07	1.384
−60.0	52.892	0.956	−27.93	241.33	1.207	1.20	3.17e+06	5.63e−07	1.378
−55.0	50.635	0.808	−34.35	241.33	1.207	1.01	3.05e+06	4.94e−07	1.306
−50.0	48.323	0.712	−41.21	241.33	1.207	0.90	3.11e+06	4.30e−07	1.000
−45.0	45.909	0.670	−47.99	241.33	1.207	0.85	3.39e+06	3.72e−07	0.926
−40.0	43.356	0.642	−54.26	241.33	1.207	0.82	3.88e+06	3.14e−07	0.897
−35.0	40.714	0.617	−59.90	241.33	1.207	0.78	4.25e+06	2.74e−07	0.872
−30.0	38.037	0.591	−64.90	241.33	1.207	0.74	4.58e+06	2.41e−07	0.846
−25.0	35.377	0.563	−69.28	241.33	1.207	0.73	5.68e+06	1.91e−07	0.819
−20.0	32.784	0.534	−73.09	241.33	1.207	0.67	5.81e+06	1.73e−07	0.796
−15.0	30.272	0.507	−76.35	241.33	1.207	0.65	6.60e+06	1.46e−07	0.776
−10.0	27.863	0.479	−79.12	241.33	1.207	0.60	6.83e+06	1.32e−07	0.761
−5.0	25.558	0.457	−81.42	241.33	1.207	0.56	6.68e+06	1.25e−07	0.749
0.0	23.339	0.438	−83.29	241.33	1.207	0.53	6.90e+06	1.15e−07	0.739

Read 3.17e+05 as 3.17×10^5.

6. Thermal Structure

6.1. Overview

The state properties determined from decelerations measured during probe entry into Jupiter's atmosphere are presented in Table 8 and in Figures 26, 27, and 28. These data are updated from those in our preliminary reports [*Seiff et al.*, 1996a, 1997a]. The variations of density, pressure, and temperature with altitude are listed at 20 km intervals in Table 8, along with mean molecular weight μ, the gas constant R, acceleration of gravity g, and ratio of specific heats c_p/c_v. The ratios of specific heats were calculated from the code of *Gierasch and Conrath* [1985], supplemented by inclusion of concentrations shown in Table 5. Heat capacities of trace constituents were evaluated at 288 K, with no temperature variation.

Densities range from $\sim 10^{-11}$ to $\sim 10^{-1}$ kg/m^3. The density scale height is relatively constant below 350 km (Figure 26). Above this, the data curve toward a much steeper slope, indicating higher temperatures. Pressures in Figure 27 have a similar variation. The threshold pressure is ~1 nbar. The value plotted and tabulated, 0.96 nbar, corresponds to an initial temperature of 900 K. For initial temperatures from 700 to 1200 K, it varied from 0.75 to 1.28 nbar.

Temperatures derived from the density and pressure profiles and the equation of state are shown in Figure 28 for the three initial temperatures, 700, 900, and 1200 K, with the gas constant defined by the composition model described above. The three initial temperature profiles converge to within ±40 K at an altitude of 750 km, and below this, the initial value chosen rapidly becomes unimportant. With T_i = 700 K, the vertical temperature gradient above 800 km indicates upward heat

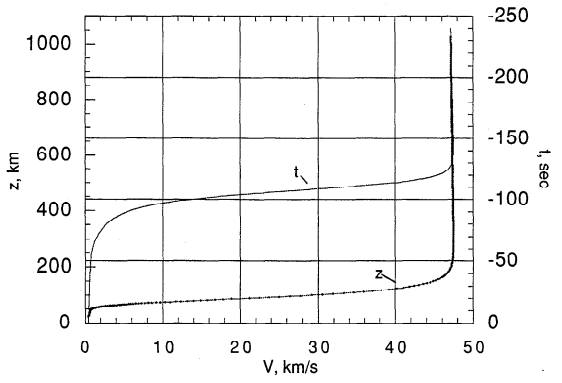

Figure 20. Probe velocity during entry as a function of time and altitude. Velocity started to decrease significantly at about −120 s (155 km), simultaneous with the onset of ablative mass loss.

conduction. At thermal equilibrium this heat must be radiated to space. With a 900 K exosphere, the vertical heat flux effectively terminates at 800 km. With 1200 K at the threshold, a constant exospheric temperature is not reached. The heating and wavelike oscillations continue to the top of the data. With either 900 or 1200 K at the top, exosphere temperatures derived from the Voyager solar and stellar occultations, 1450 ± 50 K at 1500 ± 400 km [*Atreya et al.*, 1979] or 1100 ± 200 K at 1200 ± 100 km [*Festou et al.*, 1981] roughly agree with our results. The Voyager finding of 200 ± 50 K at 400 km differs from our measurement either in temperature (by 170 K) or altitude (by 50 km, not a serious discrepancy on a planet of this size). However, the temperature deduced at 800 km by *Festou et al.* [1981], ~425 K, differs significantly, by 450 K, from our measurement at this altitude.

We attributed the oscillations of temperature with altitude to gravity waves [*Seiff et al.*, 1996a, 1997a]. Using gravity wave theory, *L. A. Young et al.* [1997] showed that two discrete vertical wavelengths, 91 and 288 km, superimposed on a mean structure, simulate the observed profile above 300 km. Furthermore, the energy viscously dissipated by these waves is comparable to that needed to heat the atmosphere. These long waves do not become statically unstable and break in the expansion phase because their lapse rates remain subadiabatic. Rather, they dissipate viscously to heat the atmosphere. Amplitudes first increase with altitude, as expected for gravity waves, reach a maximum, then diminish toward the experiment

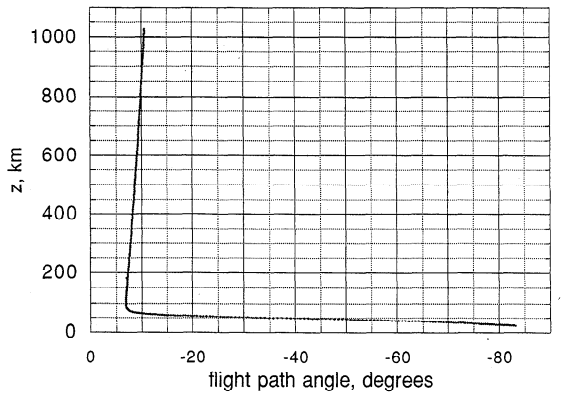

Figure 21. Probe flight path angle as a function of altitude. The trajectory remained shallow down to 70 km altitude, below which it steepened rapidly, reaching 83° at the start of descent.

threshold altitude (Figure 28) as a result of dissipation [*L. A. Young et al.*, 1997]. A more complex family of shorter vertical wavelength oscillations appears between 300 km and the tropopause (Figure 29). The shorter waves become unstable in their expansion phase and dissipate energy by breaking (L. A. Young et al., unpublished manuscript, 1998). They are fully absorbed below 300 km and do not appear at higher altitudes.

The isothermal layer in which these shorter waves reside extends from 290 to 90 km and is remarkable for its depth (Figure 29). Below this layer, temperature decreases ~1.25 K/km toward another near-isothermal layer 25 km deep just above the tropopause. The minimum temperature recorded was 107 K, but the minimum of the mean curve is close to 109 K. The location of the tropopause, which we define as the upper limit of adiabatic $T(p)$, is somewhat obscured by the noise in the temperature data, which is caused by the unsteadiness of the probe subsonic drag coefficient below 55 km altitude. This is not due to atmospheric variability. The tropopause was just above 28 km altitude at a density of 0.066 kg/m^3 and a pressure of 260 mbar, higher than the tropopause pressures reported by the Voyager infrared spectrometer (120–150 mbar). This may partly reflect a different definition of the tropopause as the point of minimum temperature, but a real difference in structure is also indicated. This could reflect conditions in a 5-μm hot spot, as compared to the north equatorial belt (NEB) generally.

Figure 30 compares our data near the tropopause with Voyager observations. There is substantial agreement from 10 to 1000 mbar. The ASI tropopause profile is similar to that seen within 1° of the equator during egress from radio occultation by Voyager 1 (Figure 30a). The smooth infrared imaging spectrometer (IRIS) sounding (Figure 30b) [*Kunde et al.*, 1982] is an average taken over the NEB with ~10 km vertical resolution, whereas the probe sounding, also in the NEB, is a local measurement in a 5-μm hot spot with ~0.5 km resolution. At pressures between 20 and 300 mbar, the IRIS average profile is ~5–10 K warmer than the probe sounding. It also differs by the absence of an isothermal region above the tropopause. The three radio occultation soundings [*Lindal et al.*, 1981] differ at pressures between 10 and 60 mbar by as much as 26 K at 30 mbar, some of which could reflect differences in phase of gravity waves. Also, as noted by Lindal, differences may reflect variability rather than scatter, since the soundings were at different local times and latitudes. The Voyager 1 ingress (Figure 30b) sounded the atmosphere in the south equatorial belt (SEB) at 11°–13°S latitude, probably the most comparable region to the Galileo site, although not in a hot spot. However, at pressures >10 mbar, the egress sounding showed the closest agreement with the probe sounding by defining a nearly isothermal layer above the tropopause, at ~117 K from 30 to 200 mbar in the Voyager 1 egress, and at ~112 K from 60 to 270 mbar in the probe sounding. Detailed structures of the two soundings within this layer are remarkably similar. The occultation temperature at 1 bar, 165–166.5 K, also agrees well with the probe value, 166.1 K. The Voyager 1 ingress sounding does not contain as deep an isothermal structure. The Voyager 2 egress sounding (not shown) was at high latitudes, 57°–73°S and, interestingly, did not disagree radically with Voyager 1 ingress [*Lindal et al.*, 1981].

Figure 29 also shows temperatures measured in the descent phase of the ASI experiment ($p > 400$ mbar) to be consistent with final temperatures in the entry phase. Densities across the experiment mode change are compared in Figure 31. This

Table 7. Descent Trajectory

p, bars	z, km	T, K	ρ, kg/m^3	g, m/s^2	dz/dt, m/s	dT/dz, K/km	t, s
0.468	17.291	130.00	0.1000	23.265			19.23
0.500	15.950	132.79	0.1046	23.266			34.28
0.600	12.094	140.84	0.1184	23.269	97.4	−2.09	75.41
0.700	8.652	148.04	0.1314	23.272	88.9	−2.09	112.41
0.800	5.528	154.57	0.1438	23.274	80.6	−2.09	148.81
0.900	2.659	160.56	0.1557	23.276	81.6	−2.09	184.60
1.00	0.000	166.10	0.1710	23.278	74.5	−2.08	218.35
1.20	−4.820	176.11	0.1892	23.282	71.7	−2.07	281.29
1.40	−9.120	184.99	0.2102	23.285	68.3	−2.06	343.34
1.60	−13.019	193.00	0.2302	23.288	63.6	−2.05	405.62
1.80	−16.597	200.31	0.2495	23.290	64.9	−2.04	460.80
2.00	−19.911	207.06	0.2682	23.293	60.4	−2.03	514.02
2.20	−23.005	213.32	0.2863	23.295	58.2	−2.02	565.00
2.40	−25.910	219.19	0.3039	23.297	56.9	−2.01	614.60
2.60	−28.652	224.71	0.3211	23.299	55.0	−2.01	662.46
2.80	−31.253	229.92	0.3380	23.301	53.2	−2.00	709.16
3.00	−33.728	234.87	0.3545	23.303	54.1	−2.00	755.34
3.20	−36.090	239.59	0.3706	23.305	51.2	−1.99	800.16
3.40	−38.352	244.09	0.3865	23.307	50.1	−1.99	844.60
3.60	−40.525	248.40	0.4021	23.308	48.7	−1.98	887.90
3.80	−42.614	252.55	0.4174	23.310	49.0	−1.98	929.10
4.00	−44.627	256.53	0.4326	23.311	48.4	−1.98	971.29
4.20	−46.572	260.38	0.4474	23.313	47.8	−1.98	1011.6
4.40	−48.454	264.09	0.4621	23.314	47.8	−1.97	1051.9
4.60	−50.277	267.68	0.4766	23.316	45.2	−1.97	1090.9
4.80	−52.045	271.16	0.4909	23.317	45.6	−1.97	1129.9
5.00	−53.762	274.54	0.5051	23.318	45.3	−1.97	1167.7
6.00	−61.692	290.10	0.5735	23.324	42.1	−1.96	1351.6
7.00	−68.744	303.88	0.6386	23.329	40.0	−1.95	1526.1
8.00	−75.117	316.31	0.7010	23.334	37.8	−1.95	1691.3
9.00	−80.952	327.67	0.7612	23.339	36.6	−1.95	1849.6
10.0	−86.346	338.16	0.8195	23.342	34.5	−1.94	2001.9
11.0	−91.370	347.92	0.8761	23.346	34.6	−1.95	2149.4
12.0	−96.081	357.08	0.9313	23.350	32.9	−1.94	2290.2
13.0	−100.52	365.71	0.9852	23.353	32.5	−1.94	2426.4
14.0	−104.73	373.87	1.0379	23.356	31.5	−1.94	2557.7
15.0	−108.72	381.64	1.0895	23.359	31.0	−1.94	2685.6
16.0	−112.53	389.04	1.1402	23.362	28.7	−1.94	2814.7
17.0	−116.18	396.13	1.1900	23.365	28.9	−1.94	2940.4
18.0	−119.67	402.93	1.2390	23.367	27.9	−1.95	3064.3
19.0	−123.03	409.46	1.2872	23.370	27.7	−1.95	3184.9
20.0	−126.26	415.75	1.3347	23.372	27.5	−1.95	3306.7
21.0	−129.38	421.83	1.3816	23.375	26.6	−1.95	3425.0
22.0	−132.40	427.71	1.4278	23.377			3520.6

density agreement was the basis for defining the ablation mass loss at the maximum bound of the uncertainty. The time of passage through the 450 km level was likewise chosen to give equal altitudes at the end of entry and the start of descent.

We combine the temperature structure defined by the two experiment modes to obtain Figure 32, yielding an overview of the thermal structure from 1 nbar to 22 bars. Figure 33 shows a similar overview of the density structure.

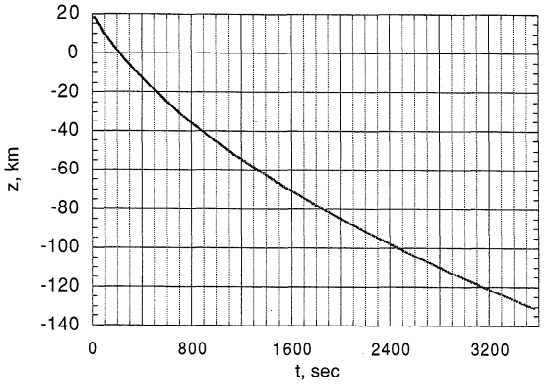

Figure 22. Probe altitude as a function of time in parachute descent.

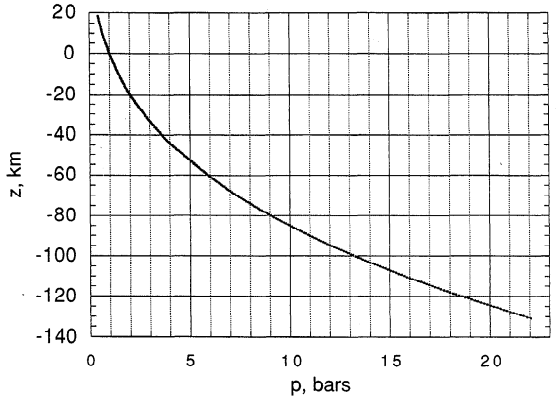

Figure 23. Altitude-pressure relationship in descent.

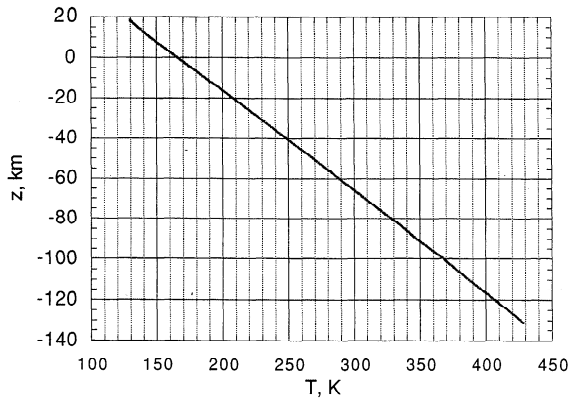

Figure 24. Temperature as a function of altitude in descent.

6.2. Lower Atmosphere Static Stability

In Figure 34 we plot temperature in the lower atmosphere as a function of pressure and compare with a dry adiabat which passes through 260 K at 4.18 bars. A line connects all the data points, with every tenth point shown as a symbol. The adiabat is indicated by a slightly heavier line. It was calculated using the code of *Smith and Gierasch* [1995; see also *Gierasch and Conrath*, 1985], with hydrogen assumed to be in ortho/para equilibrium. (At pressures greater than ~2 bars, the adiabats calculated assuming equilibrium, frozen, and "normal" ortho/para ratio (3:1) essentially coincide.) The data follow the adiabat closely except in the vicinity of 2 bars, where pressure measurement uncertainties are large (Table 4) and above ~18 bars. We conclude that the atmosphere in the 5-μm hot spot is close to dry adiabatic down to the 18 bar level, with the possibility of small deviations locally.

Enlarged sections of Figure 34 are shown in Figure 35a and 35b. At $p < 0.7$ bar, measured temperatures are above the adiabat by a maximum of 3.5 K. We believe this could be the signature of a tenuous ammonia cloud, warmed by absorption of thermal radiation from below. The temperature rise cannot be explained by heat of condensation, which would produce an increment of ~0.17 K. The measurement disagreement with the adiabat near 0.45 bar is well determined. Two pressure sensors define it at a time when sensor temperatures were within the calibration range. Also, laboratory tests indicate a delayed response when a large temperature gradient is applied to the sensors, but at 0.7 bar, where the temperature rate had increased to −4.5 C/min, it could start to affect the data. At $p_2 > 2.8$ bars, the data agree closely with the selected adiabat (Figure 34), and at $p > 4$ bars, the p_3 data continue to agree with this adiabat, demonstrating that the data early in the descent are indeed high relative to the deep-atmosphere adiabat. But uncertainties in the corrections detract from exact definition of the base of this region of higher than adiabatic temperatures.

Two other probe instruments gave possible evidence for a tenuous ammonia cloud. The probe nephelometer [*Ragent et al.*, 1996, Figure 1c; this issue, Figure 5a] reported enhanced particle counts above the 0.51 bar level. The original interpretation of the broadband infrared channel (A) of the net flux radiometer (NFR) indicated radiative warming from 0.4 to 0.6 bar [*Sromovsky et al.*, 1996, Figure 2], and the NFR found other evidence for a tenuous NH_3 cloud [*Sromovsky et al.*, this issue]. Thus observations of temperature, particle counts, and net flux concur in suggesting the presence of a tenuous cloud above the 0.51 bar level. An ammonia ice cloud with its base at 0.51 bar implies NH_3 saturation at 136.7 K and an NH_3 abundance 0.20 × solar.

Figure 35b shows in more detail the divergence of the data from the adiabat above 18 bars. Temperatures from 13 to 18 bars are above the adiabat, then fall below it increasingly, with a conspicuously different lapse rate implying stability, and there is a fairly uniform slope between 17 and 22 bars. The pressure deviation at 390 K is 200 mbar, somewhat greater than the formal measurement uncertainty. The slope change at 16 bars is sensitive to the extrapolation of sensor offset at sensor temperatures between 60° and 118°C. At 22 bars, where measured atmospheric temperature is 4 K below the adiabat, T_1 and T_2 agree within 0.1 K, and there is no known source for a 4 K temperature error. Alternatively, the pressure deviation at 422 K is approximately +0.7 bar. This is over 3 times the estimated pressure uncertainty at 22 bars, approximately ±0.2 bar (Table 4), which suggests that the deviation from the adiabat is real. A pressure error of +0.7 bar is equivalent to an offset error of 125 mV. A higher offset is required to reduce the pressure. As shown in the Figure A3, we have used the higher of the two sensor offset extrapolations in reducing the data, 44 mV greater than the Tavis (sensor contractor) estimate. An extrapolated offset of +175 mV at 118°C is required to put the measurement on the adiabat, which is off the scale used in Figure A3 and requires an inflection in the offset versus temperature curve. With this extrapolation, all pressures >15 bars would decrease by roughly $\Delta p = 0.11(p - 15)$ bars, somewhat increasing deviations of the data from the adiabat below 18 bars. Thus, while our extrapolation and the uncertainty estimates indicate static stability at pressures ≥15 bars,

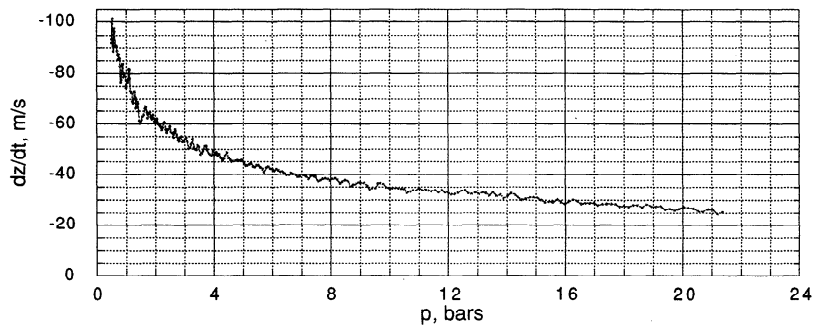

Figure 25. Probe descent velocities as a function of depth. An adiabatic temperature-pressure relationship was assumed in deriving these velocities.

Table 8. Upper Atmospheric State Properties

z, km	p, mbar	T, K	ρ, kg/m^3	μ, amu	R, J/(kg K)	g, m/s^2	c_p/c_v
1029.2	9.633e−07	899.9	2.575e−11	1.999	4159.0	22.526	1.400
1020.0	1.018e−06	903.4	2.711e−11	2.000	4157.8	22.533	1.400
1000.0	1.148e−06	897.0	3.082e−11	2.001	4155.4	22.547	1.400
980.0	1.297e−06	883.9	3.535e−11	2.002	4152.9	22.562	1.400
960.0	1.468e−06	872.2	4.057e−11	2.003	4150.5	22.576	1.400
940.0	1.664e−06	866.0	4.635e−11	2.004	4148.1	22.590	1.400
920.0	1.888e−06	865.4	5.264e−11	2.006	4145.6	22.605	1.400
900.0	2.141e−06	869.1	5.948e−11	2.007	4143.2	22.619	1.400
880.0	2.427e−06	875.2	6.700e−11	2.008	4140.9	22.633	1.400
860.0	2.749e−06	881.4	7.539e−11	2.009	4138.5	22.648	1.400
840.0	3.112e−06	885.2	8.502e−11	2.010	4136.2	22.662	1.400
820.0	3.522e−06	884.4	9.638e−11	2.011	4133.9	22.677	1.400
800.0	3.990e−06	877.2	1.101e−10	2.012	4131.6	22.691	1.400
780.0	4.527e−06	862.2	1.272e−10	2.014	4128.5	22.706	1.401
760.0	5.152e−06	840.0	1.487e−10	2.015	4125.5	22.720	1.401
740.0	5.887e−06	812.0	1.759e−10	2.017	4122.4	22.735	1.401
720.0	6.765e−06	776.1	2.117e−10	2.018	4119.3	22.749	1.401
700.0	7.827e−06	741.0	2.567e−10	2.020	4116.2	22.763	1.401
680.0	9.117e−06	712.8	3.113e−10	2.023	4110.6	22.778	1.401
660.0	1.068e−05	692.7	3.757e−10	2.026	4104.8	22.792	1.401
640.0	1.256e−05	680.2	4.506e−10	2.028	4099.1	22.807	1.402
620.0	1.481e−05	674.6	5.364e−10	2.031	4093.4	22.822	1.402
600.0	1.749e−05	669.8	6.390e−10	2.034	4087.6	22.836	1.402
580.0	2.067e−05	670.3	7.562e−10	2.039	4078.2	22.851	1.402
560.0	2.445e−05	664.0	9.053e−10	2.043	4068.8	22.865	1.403
540.0	2.903e−05	642.4	1.114e−09	2.049	4056.9	22.880	1.404
520.0	3.484e−05	594.3	1.451e−09	2.057	4042.2	22.894	1.404
500.0	4.256e−05	545.9	1.937e−09	2.064	4027.4	22.909	1.405
480.0	5.265e−05	535.8	2.455e−09	2.077	4003.9	22.924	1.406
460.0	6.518e−05	535.7	3.058e−09	2.089	3980.4	22.938	1.408
440.0	8.149e−05	483.1	4.276e−09	2.107	3946.1	22.953	1.411
420.0	0.0001072	392.9	6.989e−09	2.129	3904.6	22.968	1.413
400.0	0.0001463	370.2	1.023e−08	2.152	3863.2	22.982	1.414
380.0	0.0002107	289.2	1.917e−08	2.187	3802.5	22.997	1.429
360.0	0.0003367	231.7	3.892e−08	2.224	3738.7	23.012	1.445
340.0	0.0006036	198.6	8.251e−08	2.257	3684.5	23.026	1.461
320.0	0.001152	194.2	1.629e−07	2.281	3645.4	23.041	1.472
300.0	0.002177	177.6	3.417e−07	2.296	3621.3	23.056	1.483
280.0	0.004800	152.8	8.713e−07	2.303	3610.5	23.070	1.488
260.0	0.01094	151.0	2.012e−06	2.306	3604.8	23.085	1.489
240.0	0.02475	155.7	4.416e−06	2.308	3602.5	23.100	1.489
220.0	0.05593	157.2	9.878e−06	2.309	3601.6	23.115	1.490
200.0	0.1257	158.2	2.206e−05	2.309	3600.7	23.130	1.490
180.0	0.2824	157.4	4.984e−05	2.309	3600.6	23.144	1.490
160.0	0.6192	168.6	0.0001020	2.309	3600.6	23.159	1.490
140.0	1.342	160.5	0.0002325	2.309	3600.5	23.174	1.491
120.0	3.079	149.8	0.0005710	2.309	3600.4	23.189	1.491
100.0	7.177	158.1	0.001261	2.309	3600.4	23.204	1.493
80.0	16.40	143.8	0.003168	2.309	3600.4	23.218	1.511
60.0	43.74	122.6	0.009915	2.309	3600.4	23.233	1.534
40.0	135.8	113.2	0.03335	2.309	3600.4	23.248	1.547
23.3	351.5	122.9	0.07945	2.309	3600.4	23.261	1.528

Read 9.633e−07 as 9.633×10^{-7}.

the sensor was well beyond its calibrated temperature range during this interval, and the indicated stability is not certain. It is, however, supported by the apparent presence of gravity waves in this region, as indicated by the stability data which follow.

Lapse rates dT/dz are shown in Figure 36 as a function of pressure and compared with the adiabatic lapse rate. These were derived from the complete descent profile based on 15-point marching cubic fits to the pressure data. The small adiabatic lapse rates in Jupiter's atmosphere, $\Gamma \sim 2$ K/km, are a consequence of the large heat capacity of hydrogen and helium ($\Gamma = -g/C_p$). Two essentially independent data sets were used to derive lapse rates shown at the top and bottom of Figure 36. One uses the p_2, T_1 data at pressures below 4 bars and the p_3, T_1 data at pressures above 4 bars (upper graph); the other uses the p_3, T_2 data throughout (lower graph). Between 6 and 13 bars (290–365 K), the lapse rate is close to dry adiabatic. The upper graph shows local regions of instability at 1.7–3.5 bars and 4.2–6.3 bars, and a stable layer below the 15 bar level. The unstable layer at 2.5 bars is questionable because it is in the region of greatest pressure uncertainty. The lower graph essentially duplicates the upper graph at $p > 4$ bars. Both show a stable layer at $p > 15$ bars, and wave structure therein with vertical wavelength ~0.7 bars. While the two

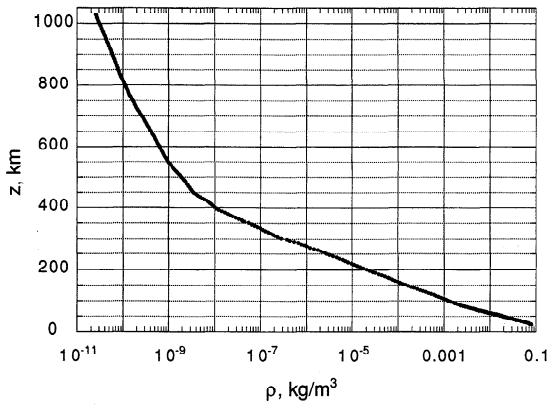

Figure 26. Density of the upper atmosphere as a function of altitude, derived from measured probe decelerations. A major change in density scale height occurred between 350 and 550 km. This coincides with the onset of diffusive separation. The steeper slope above 550 km indicates a major warming of the upper atmosphere.

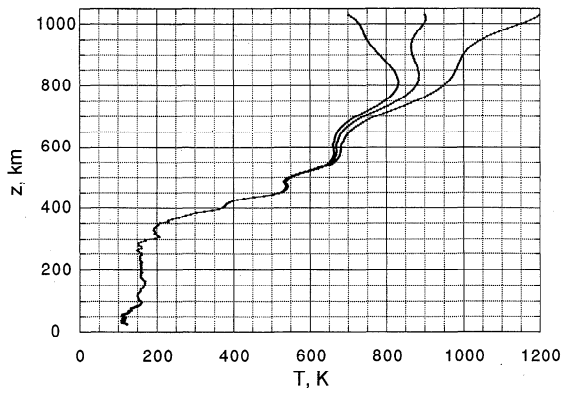

Figure 28. Temperature structure of the upper atmosphere calculated from measured densities, derived pressures, and the mean molecular weight profile of Figure 19. The effect of three widely differing temperature assumptions at the initial altitude is shown. The three profiles effectively converge at 750 km altitude. Waves in the thermal structure and the deep isothermal layer below 300 km are conspicuous.

stability curves are derived from independent sets of numbers, the two data sets differ at $p > 4$ bars only by a 2 s sampling time offset and the use of T_2 instead of T_1 temperatures. The data indicate an atmosphere close to dry adiabatic, but possibly slightly stable between 6 and 13 bars.

7. Winds and Turbulence

7.1. Winds in the Deep Atmosphere

Seiff et al. [1997b] analyzed the z axis accelerometer data in parachute descent (Figure 15) to define zonal winds in the deep atmosphere. Winds were found to increase from <100 to ~200 m/s as the probe descended from 0.4 to 4 bars, beyond which they were steady to at least the 17 bar level. Measurement resolution was coarse (1 count ~ 87 m/s), but these completely independent data support the Doppler wind measurements [*Atkinson et al.*, this issue] and add confidence that the wind variations and magnitudes found are correct.

7.2. Turbulence and Descent Velocity

The planned approach to measurement of turbulence in the atmosphere was to record statistics of the irregularities in the acceleration data during descent, as shown in Figure 17 for the lowest axial counting levels, $\pm 0.059\ g$ ($\pm 0.025\ g_j$). Similar data from the lateral axis accelerometers were discussed earlier. The probe descent velocity also gave evidence of turbulence and/or gravity waves. In Figure 25, descent velocities calculated by use of (2) for the adiabatic atmosphere which best fits measured pressures and temperatures were found to be irregular, with amplitudes approximately ± 1 to ± 2 m/s and a 6 m/s dip between 1.3 and 1.7 bars. This graph indicates a generally turbulent atmosphere with vertical scale ~0.2–0.3 bars.

The dominant error source in the velocity is the derivative dp/dt in (2), which was calculated using exact T, p points from the adiabat, taken at 1 K intervals. Times assigned to these points are those at which the temperatures (and pressures) were sampled. Descent velocities affect the times at which given temperatures are reached. Pressures were fit by marching quadratics over 7 K temperature intervals, and dp/dt was analytically evaluated at the central points of the quadratics. The finite measurement resolution in temperature ultimately affects the derivative dp/dt. We use $\delta T = \pm 0.06$ K because the reading is assigned to the middle of the count interval. The associated time uncertainty is $\delta t = \delta T/(dT/dt)$. We derived

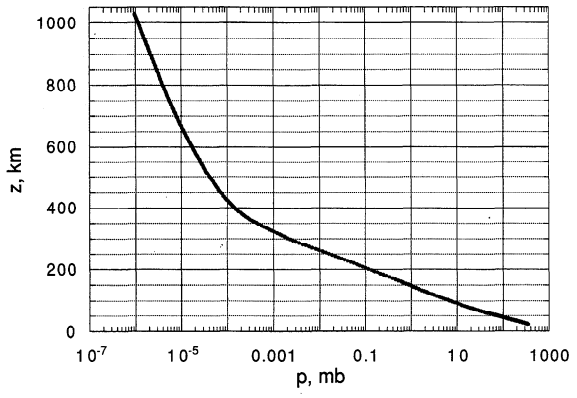

Figure 27. Pressures of the upper atmosphere obtained by integrating the densities in Figure 26 in the equation of hydrostatic equilibrium.

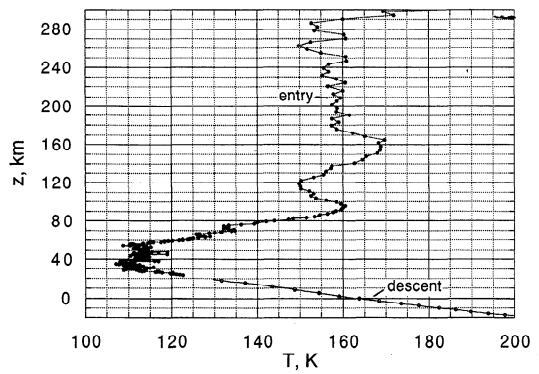

Figure 29. Expanded view of the isothermal layer and the tropopause region. Waves dominate the isothermal layer. The noisy structure in the tropopause region is partly a result of the probe subsonic buffetting accelerations.

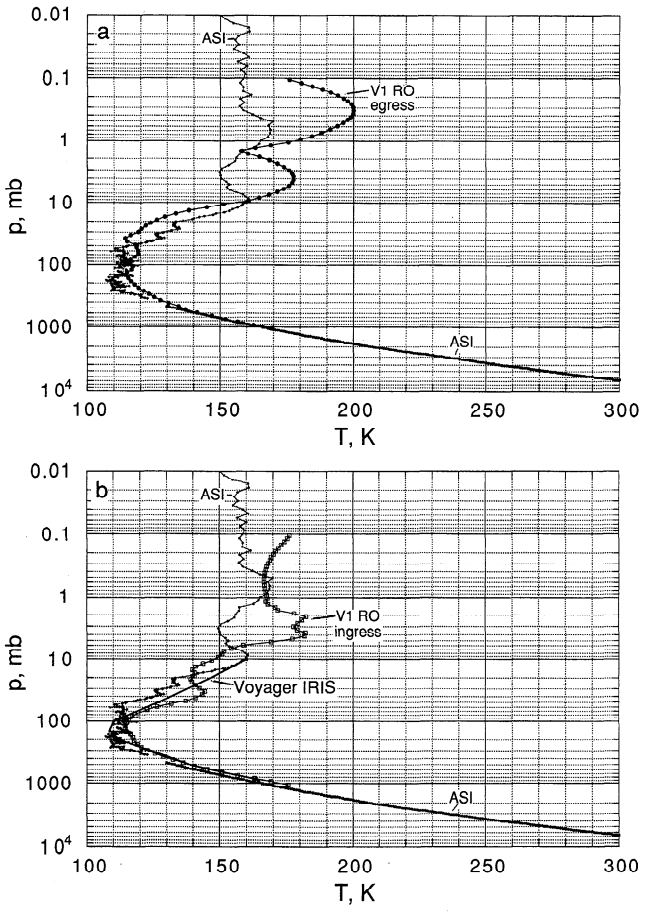

Figure 30. Comparison of the temperature profile in the tropopause region with remote sensing by Voyager 1 experiments. (a) The Voyager 1 egress data, taken within ±1° of the equator, have a similar tropopause structure to and agree very closely in temperature at 1 bar with the probe sounding. (b) The IRIS data in the NEB have a sharper temperature minimum than the ASI data. The occultation ingress, at 11°–13° latitude, is ~6 K warmer at 1 bar than the ASI 5-μm hot spot sounding.

the following relation between resolution uncertainty in temperature and uncertainty in dp/dt:

$$\delta(dp/dt)/(dp/dt) = f(\delta T/\Delta T)$$

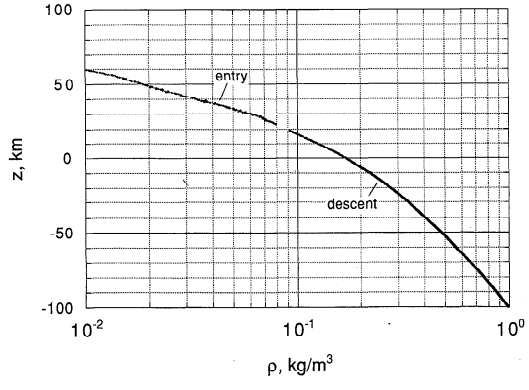

Figure 31. Continuity of the density data from measured accelerations during entry and from measured pressures and temperatures in descent.

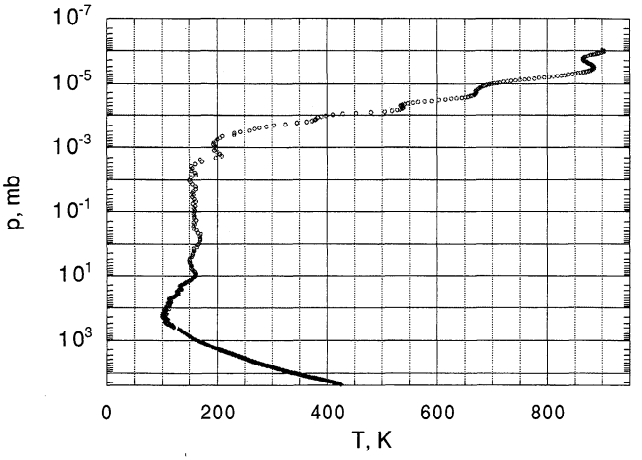

Figure 32. Complete temperature structure of the atmosphere within a 5-μm hot spot measured by the ASI experiment.

where δT is defined above and $\Delta T = 6$ K over the 7-point temperature interval for which we make a marching polynomial fit to $p(t)$. The factor f is the statistical advantage of using 7 temperature points over using just the two end points. This factor was determined by a Monte Carlo analysis with 1000 trials to be 0.34, rms, for 7 points. The fractional uncertainty in the pressure gradient, which approximates the fractional uncertainty in descent velocity, is thus constant at $0.01 \times 0.34 = 0.0034$. The velocity uncertainty magnitude thus varies from ±0.3 m/s at 90 m/s to ±0.1 m/s at 30 m/s. This is much smaller than the velocity fluctuations in Figure 25, which indicates that finite resolution is not the source of the fluctuations.

Descent velocities were also derived directly from the pressure-temperature data points. The pressure data were fitted with quadratic and cubic polynomials over marching multipoint intervals to define dp/dt at the central point. We tried intervals of 7, 9, 11, and 15 points to see how this selection affected the velocities. The velocities obtained, e.g., Figure 37, differ from those in Figure 25 by up to a few m/s wherever the data deviate from the adiabat. In Figure 37, we compare results from quadratic and cubic fits over 15-point intervals, used to suppress pressure-measurement resolution uncertainty. Correlation coefficients of the fitted equations with the pressure data are typically 0.9999. The initial hump in the descent velocity, above the 1 bar level, may be spurious. This is indicated by the

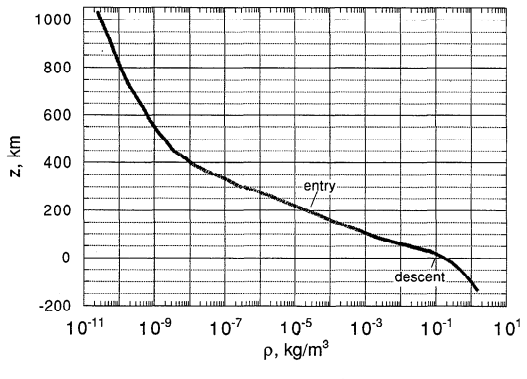

Figure 33. Density structure of Jupiter's atmosphere from 1029 km above to 132 km below the 1-bar level.

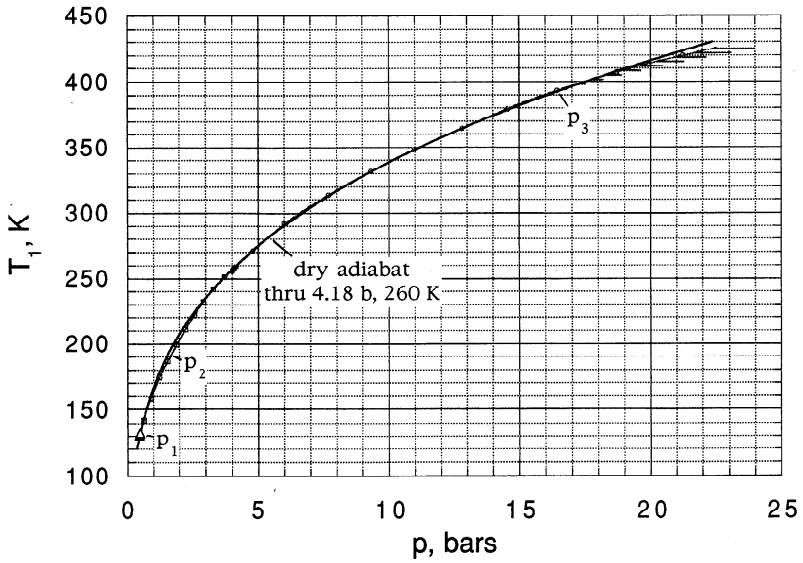

Figure 34. Temperature as a function of pressure below the level of the clouds, compared with an equilibrium adiabat which passes through 260 K at 4.18 bars. The data points are connected to form a continuous line, with a symbol shown at every tenth point. The adiabat is a separate line.

unreal horizontal winds required to accommodate it (D. Atkinson, private communication, 1998). It could be a result of the onset of temperature-rate effects on the pressure data. Turbulent fluctuation amplitudes derived from the data are larger than those derived from the adiabat. At $p < 2.5$ bars, the descent was fairly smooth except for the "hesitation" at 1.1–1.35 bars, the level of the cloud seen by the nephelometer [*Ragent et al.*, this issue]. This nearly coincides with the dip seen in Figure 25.

The fluctuations from cubic and quadratic fits agree well in phase and waveform, but amplitudes were generally larger with cubic smoothing than with quadratic. Cubic curve fits follow inflections in the data which the quadratic fits cannot follow. A descent velocity is derived for each data point, at time separations of 4 s. As can be seen in the figure, the oscillations thus involve coherent behavior at several (up to eight) data points, and do not simply mirror the scatter of individual measurements.

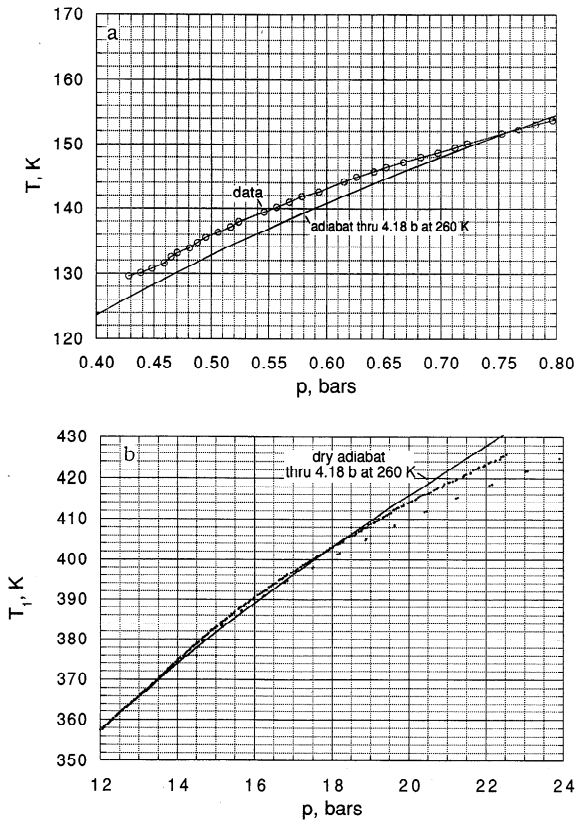

Figure 35. Expanded sections of Figure 34 at (a) $p < 0.8$ bars and (b) $p > 12$ bars.

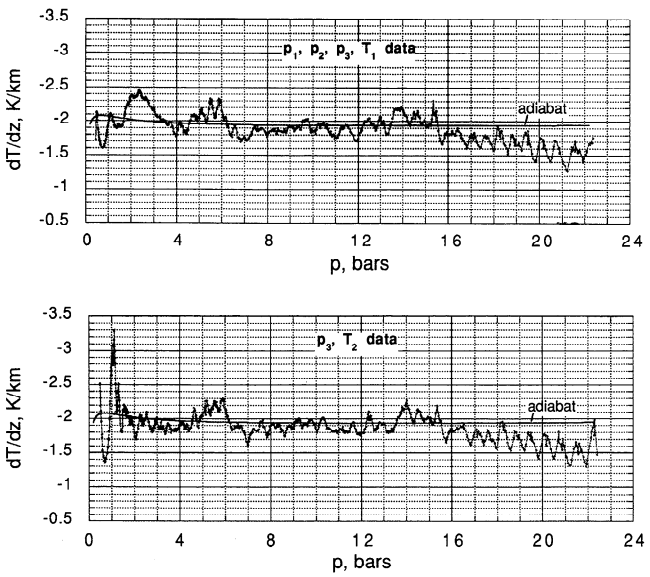

Figure 36. Atmospheric lapse rates derived from measured pressures and temperatures, compared with adiabatic lapse rate for equilibrium ortho/para hydrogen. The upper curve is from the p_2, p_3, T_1 data; the lower curve from p_3, T_1 data.

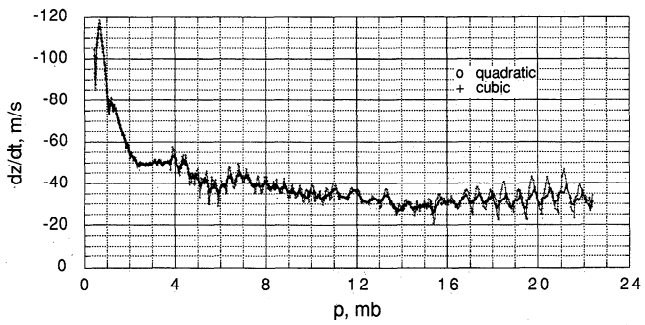

Figure 37. Descent velocities as a function of altitude and of pressure, derived from the p_2, p_3, T_1 data. To derive dp/dt for this purpose, polynomials of second and third degree were fit to 15 consecutive pressures; dp/dt was the polynomial slope at midpoint. Second degree fits are circles; third degree fits are plus signs.

The effect of finite measurement resolution on these results was evaluated by doing a Monte Carlo calculation in which random errors ≤0.5 count were assigned to data points along a quadratic $p(t)$. This produced a synthetic data set with scatter comparable to that in the data. Quadratic fits to these "data points" were then made, and midpoint slopes were compared to the exact, input slopes. The root-mean-square slope error of 1000 such random error simulations was 0.24 × the extreme slope uncertainty which used only the end points (and is easy to evaluate). Based on this exercise, we estimated the rms uncertainties in velocity to be ±0.86 m/s at 0.5 bar, ±0.15 m/s at 2 bars, ±0.013 m/s at 10 bars, and ±0.005 m/s at 22 bars. Thus resolution uncertainty will not explain the velocity fluctuations.

The velocity fluctuations in Figure 37 are, however, larger than those in the Doppler data of *Atkinson et al.* [1996, 1997, this issue]. In the Doppler analysis, horizontal winds were represented by a smooth sixth-order polynomial function $u_w(p)$. Doppler residuals, representing the lack of fit of the smooth wind profile to the data, show long-period fluctuations typically equivalent to 0.5–1 m/s velocity amplitude with vertical wavelength in pressure coordinates of ~5 bars [*Atkinson et al.*, this issue]. There are also short-period fluctuations of ~0.25 m/s with vertical wavelength ~0.2 bar, which become more regular at $p > 16$ bars. These features are similar in vertical scale to those in Figure 25 but are much smaller in amplitude. The ASI data in Figure 37 show even larger amplitudes and vertical scales ~0.4 bars. The largest Doppler residual occurs at 1.3 bars, the location of the hesitation in descent velocity seen by the ASI, where there is a >2 m/s spike in the Doppler residuals. This hesitation is also prominent in the horizontal velocity data from Earth-based tracking of the probe radio signal by the very large array (VLA) in New Mexico [*Folkner et al.*, this issue]. This feature is therefore verified by data from three experiments.

The VLA also saw fluctuations in the horizontal wind velocity of approximately ±5 m/s starting at pressures >2.5 bars. Turbulent fluctuations start at 3 bars in the ASI descent velocities and reach large amplitudes at 3.8 bars. In the Doppler tracking from the orbiter, fluctuations in horizontal wind and probe descent velocity could not be differentiated. The occurrence of simultaneous horizontal and vertical wind fluctuations could partially explain the observational differences, particularly if horizontal and vertical fluctuations are correlated. The contribution of horizontal and vertical winds to the Doppler measurement is given by

$$V_D = (u + u') \sin \beta + (w_p + w_p') \cos \beta$$

where V_D is the velocity measured by the Doppler, u is the horizontal wind, w_p is the probe descent velocity, primes indicate fluctuating components, and β is the probe aspect angle, the angle between the Doppler line of sight and the vertical. If

$$u' \sin \beta = -w_p' \cos \beta$$

no fluctuation would be detected by the Doppler experiment. Such correlations might occur with convection cells or with gravity waves propagating along inclined paths. For $\beta = 0.1$ radian, roughly 1 m/s in w_p' is equivalent to ~10 m/s in u', which is the order of magnitude of the horizontal fluctuations seen with the VLA from Earth. However, this explanation is not entirely satisfactory, since β varies during the descent, so that cancellation of fluctuations should not always occur.

A separate consideration is the reality of the departures from the adiabatic velocity profile which occur locally near 2 bars, where the pressure uncertainty is large, at 5.5 bars, and at 7 bars (compare Figures 25 and 37). When we use the descent velocities from the p-T data (Figure 37), as input to the Doppler wind retrievals, the horizontal winds rise to a peak of 340 m/s at 1 bar, drop to 90 m/s at 3 bars, rise to 180 m/s at 10 bars, and gradually decrease to 150 m/s at 22 bars, illustrating the sensitivity of the horizontal wind retrieval to accurate descent velocities. These winds disagree with those obtained from the ASI accelerometers [*Seiff et al.*, 1997b] and are less credible than those obtained with the adiabatic velocity profile used in the published Doppler wind retrievals. This exercise casts serious doubt on the deviations from the dry adiabat shown in Figure 36 at 2.5 and at 5.5 bars.

Are the descent velocity observations and the accelerometer turbulence data consistent? By taking the point-to-point derivatives of the velocity data from the quadratic and cubic fit equations, we obtained the time series of vertical accelerations shown in Figure 38, which are compared with the counting levels of the turbulence counter. With quadratic fits to $p(t)$, the accelerations are generally too low to have been counted. With cubic fits, the descent velocity data agree remarkably with the counter data, in that they make numerous crossings of level 1 ($0.059\, g_E$), less frequent crossings of level 2 ($0.118\, g_E$), and no crossings of levels 3 ($0.236\, g_E$) and 4 ($0.474\, g_E$). The velocity data do not show as many level crossings as the counter, as they do not detect higher frequencies. (The turbulence counters can register up to 4096 counts in 96 s, or 42 Hz. The largest count number recorded in a sample interval with the parachute fully open and stabilized was 306, corresponding to a frequency of 3.19 Hz, a period of 0.31 s, and a scale of 12.5 m. The 4 s sampling of the pressure data prevents the detection of fluctuation periods less than ~10 s or 0.1 Hz (vertical scales <300 m at 30 m/s descent speed).) The distribution of the accelerations derived from the cubic fit velocity data is shown in Figure 39. It has a sharp peak at perturbations <0.1 m/s^2, with <1% at or above the turbulence counter level 2. Thus the measured accelerations are consistent with the velocity amplitudes derived from the cubic fit to the pressure data.

The data from the lowest counting levels of the axial acceleration perturbation counter (Figure 17) indicate fluctuations about a factor of 3 greater than experienced in parachute drop

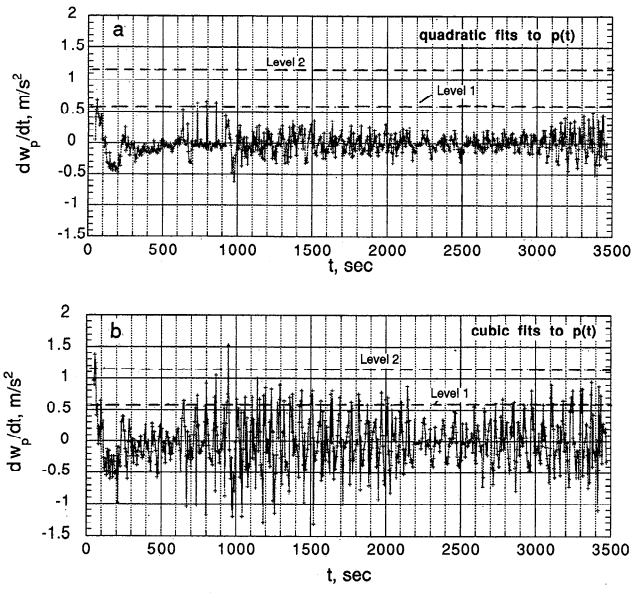

Figure 38. Vertical accelerations obtained from point-to-point derivatives of descent velocities in Figure 37. (a) Second-degree polynomial fits to $p(t)$. (b) Third-degree fits.

tests in Earth's atmosphere. The source of the turbulence could be either the relatively strong horizontal winds detected during the probe descent at Jupiter [*Atkinson et al.*, 1996, 1997, this issue; *Folkner et al.*, 1997; *Seiff et al.*, 1997b], because turbulence may be produced by Reynolds stresses that result from shear in the wind profile [e.g., *Townsend*, 1976], or it could also result from strong vertical convective motions, which are characteristically turbulent. There is also a possible input from unsteady drag of the parachute. These data will require further study.

In retrospect, the lateral turbulence counter thresholds selected were low. The normal acceleration was an absolute magnitude measurement, independent of direction. At Jupiter the highest threshold ($0.048\ g_E$) always had the largest number of counts, and during periods of valid data, the acceleration maxima (Figure 14) reached the level of $\sim 0.09\ g_E$. These data have been interpreted to indicate that the probe swung as a pendulum under the parachute, causing a component of gravity acceleration to be read by the lateral sensors. An amplitude of $0.09\ g_E$ corresponds to $\sim 2.2°$ swinging amplitude [*Seiff et al.*, 1996a]. At the calculated period of ~ 5 s, these should have registered 2 counts/cycle or 38 counts on the $0.048\ g_E$ level in a 96 s sample. The actual number of counts registered in the highest threshold was typically 40–60. These lateral turbulence acceleration levels were at least twice those observed during the drop tests at Earth, where the gravity acceleration is smaller by a factor of 2.5 and the presence of swinging oscillations was not reported. In the lower counting levels, 0.004 and $0.012\ g_E$, very few counts were registered. This would occur if the swinging oscillation were elliptical with a minimum amplitude between 0.012 and $0.048\ g_E$ (angles between 0.3° and 1.1°), so that the normal acceleration seldom fell below the second level.

Small-scale turbulence can also be deduced from the individual time series of temperature, pressure, and acceleration recorded during the descent of the Galileo probe. As noted earlier, an initial look at the T_1 temperature measurements suggests a smooth variation with time (or altitude), without indications of turbulent variations that anywhere exceed the experiment's digital resolution of 0.12 K. An analysis was done in which, first, the missing T_1 samples every 64 s, due to acquisition of calibration data, were filled, using quadratic and cubic interpolation. Then dT/dt was calculated, and its deviations from a smoothed value were obtained. Except for isolated samples near 400, 850, and 1450 s, no significant deviations from a smooth rate of temperature increase were found. However, during the final 500 s of data, the shape of the smoothed curve is poorly defined because of the relatively slow rate of temperature increase and the digitization uncertainty of the experiment. It is thus indicated that turbulent fluctuations evident in the fluctuating velocities and accelerations did not result in significant temperature fluctuations. This is to be expected in an adiabatic atmosphere, where temperatures of vertically displaced fluid parcels are the same as in the background atmosphere.

8. Discussion of Results

8.1. Waves in the Middle and Upper Atmosphere

In Figure 29, temperature fluctuations appear just above the tropopause and in Figure 28 they continue to the highest altitude measured by the ASI. In the stratosphere these fluctuations are a complex spectrum of wavelengths, and the thermal gradient often approaches, but does not cross, the adiabatic gradient, characteristic of breaking gravity waves. Similar fluctuations in the upper stratosphere of Neptune, detected by stellar occultations [*Roques et al.*, 1994], have also been interpreted as breaking gravity waves. For a wave to break in the upper stratosphere, it must be critically damped by the eddy viscosity κ [*Lindzen*, 1981]. These waves are overdamped in the thermosphere, where molecular viscosity dominates over eddy viscosity, and dissipate within two scale heights above the homopause. If the vertical wavelength is much smaller than both the horizontal wavelength and the scale height, the condition for breaking waves is that

$$\omega c^3 = 2H\nu N^3 \qquad (10)$$

where ω is the period, c is the horizontal phase speed, ν is the kinematic viscosity in the stratosphere, N is the Brunt-Vaisala frequency, and H is defined by $[\partial \ln (T^2N^3/\rho)/\partial z]^{-1}$ and reduces to the scale height in an isothermal atmosphere [*L. A. Young et al.*, 1997]. The horizontal phase speed c can be determined from the vertical wavenumber k_z by the dispersion

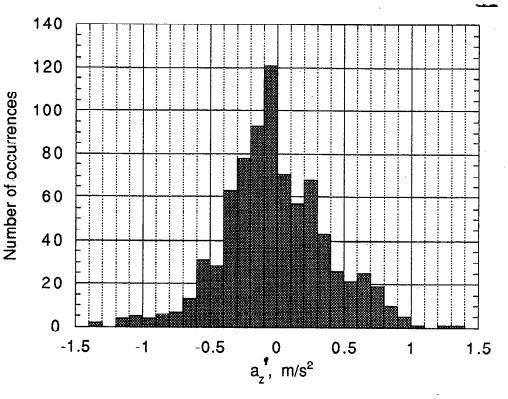

Figure 39. Frequency distribution of acceleration perturbations a_z'. Most of the perturbations are 0.1 m/s^2 or less, and only a few exceed 1 m/s^2.

relation $k_z = -N/c$. For the family of waves that break at a given ν or κ, the period is proportional to c^3, and the horizontal wavelength is proportional to c^4. If we take the 100–300 km region to be roughly isothermal at 160 K, then $N = 0.01518$ s^{-1}. Waves with vertical wavelengths of 10 and 25 km will have horizontal phase speeds of 24 and 60 m/s, periods of 0.28 and 4.4 hours, and horizontal wavelengths of 25 and 950 km, respectively.

Long-wavelength temperature fluctuations are easily seen in the thermosphere, at altitudes higher than 400 km above the 1 bar level. These fluctuations consist of a simpler wave spectrum than in the stratosphere, superimposed on an overall increase in the background temperature. Unlike in the stratospheric waves, the thermal gradients are always subadiabatic. These are not breaking waves. Their persistence into the upper thermosphere, with its higher viscosity, implies that these waves are not the continued propagation of breaking waves from the stratosphere.

Subtracting an estimate of the mean profile, we are left with a temperature fluctuation of roughly 25–40 K in the thermosphere, which can be reproduced by two upwardly propagating gravity waves which reach their maximum amplitudes at 430 and 710 km. For the wave that peaks at 430 km, we can apply the same equations that we used in the stratosphere, to find that a wavelength of 92 km implies a wave with $c = 200$ m/s, a period of 17.6 hours, and a horizontal wavelength of 12,693 km. However, for the wave that peaks at 710 km, the horizontal motion of the probe introduces some ambiguity into the interpretation of the observed vertical wavelength of 288 km. If we assume the same phase speed for both waves, then the upper wave has an actual vertical wavelength of 149 km, a period of 1.1 hours, and a horizontal wavelength of 773 km [*L. A. Young et al.*, 1997].

8.2. Heating of the Upper Atmosphere

Under the assumption of a steady state atmosphere, there is a balance between the heating rate Q, the cooling rate L, and the transport of energy by thermal conduction, so that

$$Q - L = -\partial(\kappa\, \partial T/\partial z)/\partial z \qquad (11)$$

where $\kappa = AT^s$ is the thermal conduction, $s = 0.75$ and $A = 252$ erg/(cm s $K^{-(s+1)}$). In the stratosphere, radiative heating and cooling dominate the balance. In the thermosphere the densities are low, and most radiatively active species decrease above the homopause due to molecular diffusion. The energy equation then becomes a balance between heating sources and thermal conduction.

For all choices of the temperature at experiment threshold, T_i, the upper atmosphere shows a large temperature increase below 600 km, with temperature gradients reaching 2.9 K/km, which indicates a downward energy flux of 0.53 erg/cm^2/s. This must equal the column-integrated heating rate in the thermosphere. For our favored initial temperature of 900 K, the thermal gradient decreases steadily throughout the thermosphere probed by the ASI, implying a distributed energy source. It is impossible to say if the gradient is still positive at the first temperature measured by the ASI, not only because of the uncertainty in the initial temperature, but also because of the difficulty in differentiating the mean thermal profile from any waves superimposed. The waves described in the previous section carry the required amount of energy and are able to reproduce the observed thermal profile [*L. A. Young et al.*, 1997]. Other suggestions for the heating source include Joule heating [*Clarke et al.*, 1987; *Nishida and Watanabe*, 1981], and charged particle precipitation [*Waite et al.*, 1997].

8.3. Deep Isothermal Layer

A deep isothermal layer at approximately 160 K extends from about 12 to 0.003 mbar (90–290 km altitude), from just above the tropopause to the mesopause. Wavelike oscillations in temperature with vertical wavelengths between a few kilometers to about 80 km are observed in and below the isothermal layer, but wavelengths less than 50 km are not seen above the isothermal layer [*Seiff et al.*, 1997a]. In addition, the wave amplitudes have an rms fluctuation of about 5 K throughout the isothermal layer, instead of growing inversely with the square root of the density. Clearly, these waves are absorbed in the isothermal region. In Earth's stratosphere, damping of similar waves is an important source of momentum deposition, and this may be the case on Jupiter as well. Furthermore, heating associated with wave absorption may be important for the energetics of Jupiter's stratosphere, which otherwise would be a balance between radiative heating and radiative cooling. At its upper boundary this layer also receives heat conducted downward from the thermosphere and exosphere.

8.4. Static Stability

The static stability of Jupiter's atmosphere is a fundamental property which determines the kinds of dynamical behavior that can exist. Static stability is defined by the temperature lapse rate dT/dz. If the lapse rate is greater than the adiabatic temperature gradient, $\Gamma = -g/C_p$, the atmosphere is statically unstable; if it is equal to the adiabatic lapse rate, stability is neutral; and if less than the adiabatic lapse rate, the thermal structure is statically stable. Negative or neutral static stability implies the existence of thermal convection. Positive static stability inhibits convection, and the atmosphere is stable against vertical overturning. In all our discussions of static stability, the mean molecular weight is assumed constant, and hence possible contributions to static stability from molecular weight gradients are neglected.

It was known from remote sensing observations that the atmosphere above the tropopause, about the 150 mbar level (260 mbar in the 5-μm hot spot), is stably stratified [*Kunde et al.*, 1982; *Eshleman et al.*, 1979]. No prior measurements had been made below the 1 bar pressure level. The standard assumption, based on the knowledge that Jupiter has an internal heat flux ~5 W/m^2, has been that below about 1 bar the temperature follows an adiabatic profile and the internal heat is carried outward by convection (e.g., the radiative convective equilibrium models of *Appleby and Hogan* [1984]). However *Guillot et al.* [1994] have shown that deep in the atmosphere near the 2000 K level, a statically stable layer should exist in which vertical energy transport is predominantly by radiation. Interestingly, they also show that if there are no water clouds, there is a region in the atmosphere between about 200 and 400 K in which the atmosphere becomes stable. The probe entered such a cloud-free region, and our data suggest the possibility of a slightly stable region between 290 and 365 K (6 to 12 bars) and an increasingly stable layer at temperatures between 395 and 426 K (15 and 22 bars). *Ioannou and Lindzen* [1993a, b, 1994] have computed the gravitational tides raised in the Jovian atmosphere by the moon Io and indicated that if the static stability is positive in the deep atmosphere, there is a large atmospheric response to the gravitational tide. Dynamical con-

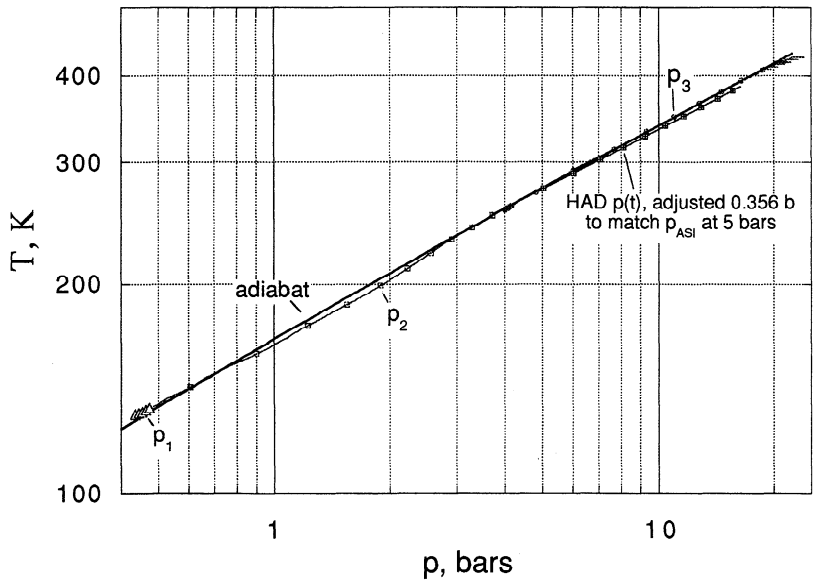

Figure 40. Difference in atmospheric stability for $T(p)$ determined from ASI pressure sensor data and HAD pressure sensor data. With the ASI data, the atmosphere is close to dry adiabatic at pressures <15 bars. With the HAD pressure data, the atmosphere is stable by ~0.06 K/km.

siderations lead to the expectation that the Jovian atmosphere is slightly statically stable below the ammonia cloud deck, probably extending down to at least several bars [*Flasar and Gierasch*, 1986; *Allison*, 1990; *Allison and Del Genio*, 1995]. The fact that considerable wind shear exists between cloud levels and about 4 bars [*Atkinson et al.*, 1996, 1997, this issue; *Seiff et al.*, 1997b; *Folkner et al.*, 1997] implies a static stability which is at least slightly positive so that dynamic instabilities do not grow and destroy the shear. The question is, How deep is the atmosphere statically stable? If the answer is very deep, as *Ioannou and Lindzen* [1994] suggested, the interior heat flux of Jupiter might then be carried out in a number of isolated thermal plumes, rather than by a global-scale convective pattern, and the driving mechanism for the zonal winds might be the gravitational tides rather than solar and internal heating [*Ioannou and Lindzen*, 1994].

One of the primary objectives of the ASI experiment was to determine the static stability of the atmosphere over the entire range of heights for which temperature was either directly measured during probe descent, or inferred from probe accelerations during entry. As discussed above, probe interior temperatures and rates of change of temperature during descent were outside preflight spacecraft specifications and caused the pressure sensors to be outside preflight calibration ranges. The extensive postencounter recalibrations and testing on flight spare and engineering units have been used to derive the pressures from the flight sensors presented earlier, yielding the stabilities shown in Figure 36. But within 2 months after encounter, prior to having conducted the additional testing and analysis of the ASI pressure sensors, pressures measured by the helium abundance detector (HAD) were used to guide selection of ASI sensor offsets at pressures greater than 5 bars. The ASI pressures obtained by reference to the HAD pressures are higher than ASI pressures derived as reported herein [*Seiff et al.*, 1996a], and the difference increases with increasing atmospheric pressure. Use of these early pressure data implied a stable atmosphere [*Seiff et al.*, 1996a].

Figure 40 compares the final ASI temperature-pressure data (p_1, p_2, p_3, T_1) with ASI temperatures analyzed with HAD pressures, which extend from 5 to 16 bars and were used by *Seiff et al.* [1996a] to guide early selection of pressure offsets. The latter data are simply labeled HAD. Note that the HAD data have been offset by 0.356 bar to agree with ASI pressures at 5 bars. For a hydrostatic atmosphere the slopes of these data define atmospheric lapse rate (4). In ln T versus ln p coordinates the dry adiabat is a straight line. The data are compared with the same dry adiabat used earlier, which passes through the (T, p) point of 260 K at 4.18 bars for the composition of the atmosphere measured by the Galileo probe neutral mass spectrometer (NMS) [*Niemann et al.*, 1996, this issue]. At temperatures shown in Figure 40 the differences in adiabats calculated from an ortho/para hydrogen ratio that is in equilibrium, or the asymptotic high-temperature ratio of 1:3, makes a difference of only tenths of a percent at most in the adiabat slope. With the ASI pressures, the ASI $T(p)$ curve closely follows the adiabat to pressures of about 15 bars, except between 0.8 and 3 bars, where the deviations are comparable to the pressure uncertainty. Note that the data expressed as lapse rates indicate the atmosphere is slightly stable from 6 to 13 bars (Figure 36). At pressures greater than 15 bars the ASI data indicate a significant subadiabatic temperature gradient by up to 0.5 K/km at 22 bars. However, as pressure increased from 15 to 22 bars, the sensor temperature increased from 65° to 118°C, and calibrations were extrapolated, which introduces uncertainty. But gravity waves require a stable atmosphere, and the apparent detection of gravity waves at these pressures reinforces the indication of stability.

The curve labeled HAD is slightly stable at all pressures, by about 0.06 K/km. Which curve represents the actual atmosphere? Unfortunately, this cannot be resolved at the present time and is not likely to be unambiguously resolved ever. There is simply no way to retest and recalibrate the entire set of hardware systems involved in each measurement; they are now part of Jupiter's atmosphere. We made extensive thermal sim-

ulation tests of the ASI flight spare and engineering pressure sensors (Appendix B), and limited tests of the HAD engineering pressure sensors, which indicated that they would not have been affected by the thermal environment to which they were exposed. The electronics that supply power to the HAD sensors and amplify the pressure signal have not been retested for the thermal regime they encountered in the probe interior. The HAD pressure electronics were adversely affected by the severe cooling early in the descent [*von Zahn et al.*, this issue], but the designers and experiment team believe that no degradation occurred during the descent into the deeper atmosphere [*von Zahn et al.*, this issue and private communication, 1997].

8.5. Nature of the 5 μm Hot Spot

The Galileo probe descended into one of the infrared bright regions in the NEB known as a 5-μm hot spot. Earth-based images of Jupiter around December 7, 1995, show that the probe entry site was near the southern edge of an intense region of 5-μm emission, well within a broader region of less intense emission [*Orton et al.*, this issue]. The hot spots are clearings in Jupiter's atmosphere through which we see to greater depth; the radiation emerging from the hot spots arises from deeper, hotter regions of the atmosphere, accounting for the enhancement in 5-μm intensity. *Ortiz et al.* [this issue] estimate that the 5-μm hot spots comprise about 15% of the NEB. There are about 12–15 hot spots approximately regularly spaced around a latitude circle [*Smith et al.*, 1979; *Owen and Terrile*, 1981; *Hunt et al.*, 1981]. The regularity of spacing suggests that the hot spots might be related to either a planetary wave or a convective phenomenon. Frequently, there is a convective plume associated with a hot spot, the tail of which moves toward the equator. Hot spots move zonally with the speed of the top of the visible cloud deck, given by *Ortiz et al.* [this issue] as 103 m/s. In contrast, the wind speeds inferred from the Galileo probe data increase from ~100 to ~200 m/s between pressure levels of 1 and 4 bars [*Atkinson et al.*, 1997; *Folkner et al.*, 1997; *Seiff et al.*, 1997b]. Consequently, vertical flows must be sheared in the windward direction by the increasing velocity of the atmosphere with depth down to the 4 bar level, and be continually stretched by the much higher velocities than the hot spot below the 4 bar level.

It has been suggested that the 5-μm hot spots are huge downdrafts of dry atmosphere that may have originated from upwellings around the hot spots [*Niemann et al.*, 1996; *Showman and Ingersoll*, 1998; *Atreya et al.*, 1997]. Water vapor in the upwelling atmosphere would condense, leaving dry atmosphere to complete the return downflow in the hot spot. However, removal of water vapor from a parcel of Jovian atmosphere makes the parcel less dense than moist atmosphere, and dry buoyant atmosphere will resist sinking. Condensation of water vapor also releases latent heat, warms the dried atmosphere, and further enhances its buoyancy. *Gierasch and Conrath* [1985] have estimated the buoyancy induced by condensation in the Jovian atmosphere. They show that $\Delta T/T = \Delta\theta/\theta$ (T is temperature and θ is potential temperature) at the condensation level is about 10^{-2} for a solar abundance of condensing water, leading to a $\Delta\theta$ of about 1 K.

A simple calculation demonstrates that it would be extremely difficult for an isolated forced downdraft with this amount of buoyancy or increased potential temperature to penetrate to the 15 bar pressure level. With dissipation and radiative effects neglected (the radiative timescale is very large in this region of the atmosphere), potential temperature will be a conserved property in a dry downdraft. If the downdraft is steady, Bernoulli's law along a streamline of a perfect gas is [*Batchelor*, 1967]

$$q^2/2 + c_pT + gz = \text{const} \tag{12}$$

where q is the magnitude of the velocity and includes the contributions from both the vertical and horizontal components of the wind. By using the expression $T = \theta(p/p_0)^\kappa$ for potential temperature in terms of T and p, where $\kappa = R/c_p$, and noting that the temperature increases with depth at the rate g/c_p along a dry adiabat (constant θ), we can rewrite (12) as

$$q^2/2 + c_p\Delta\theta(p/p_0)^\kappa = \text{const} \tag{13}$$

where θ has been expressed as $\theta_{bg} + \Delta\theta$, θ_{bg} is the potential temperature of the background atmosphere, $\Delta\theta$ is the potential temperature difference between atmosphere in the downdraft and in the surroundings, the term $c_p\theta_{bg}$ has been included in the constant on the right side of the equation, and p_0 is the pressure at the reference level. If the downdraft is forced with speed q_0 at the reference level, taken here as the cloud tops where $p_0 = 0.2$ bar [*West et al.*, 1986], then according to (13), the downdraft will penetrate only to the depth p_d because of its positive buoyancy, i.e., q will be zero when $p = p_d$, where

$$p_d/p_0 = \{1 + q_0^2/(2c_p\Delta\theta)\}^{1/\kappa} \tag{14}$$

For $\Delta\theta = 1$ K, estimated above and $q_0 = 10$ m/s (a large downflow speed), (14) gives $p_d = 0.203$ bar, i.e., the downflow would be brought to rest almost immediately. For $\Delta\theta = 0.0015$ K and $q_0 = 10$ m/s, (14) gives $p_d = 17$ bars, i.e., only if the air had a very small buoyancy or $\Delta\theta$ could it be forced down to the levels probed.

The above calculation considers the buoyancy from condensation warming but not the density change associated with moisture depletion, which makes it even more difficult to force atmosphere downward in the hot spot to pressure levels reached by the probe. If the atmosphere were slightly statically stable as suggested by the HAD measurements or if it were stable at pressures in excess of about 15 bars as suggested by the corrected ASI pressure data, then the difficulty of forcing dry atmosphere downward would be exacerbated. Clearly, upwelling atmosphere cannot be immediately forced downward in a hot spot. Before descending into a hot spot the atmosphere must lose essentially all of its buoyancy, perhaps by radiative cooling as it travels horizontally toward the hot spot from large distances. Cloud tracking has indicated that the convergent or eddy part of the horizontal wind field is about a few meters per second [*Ingersoll et al.*, 1981]. Recent observations by the Galileo solid-state imaging instrument revealed horizontal winds of 10–30 m/s converging into a hot spot (A. R. Vasavada et al., Galileo imaging of Jupiter's atmosphere: The great red spot, equatorial region, and white ovals, submitted to *Icarus*, 1997). However, there is no information on the magnitude of the vertical wind, and preliminary interpretation of the ASI data indicates alternating intervals of upwelling and downwelling of the vertical winds at the Galileo probe site. Observations of the vertical flow in 5-μm hot spot regions on Jupiter would provide important constraints on hot spot models.

Thermodynamic inference from the Galileo probe data requires the atmosphere in the hot spot to be less dense than the surrounding atmosphere at pressures above 5 bars; the hot

spot atmosphere could be lighter than its surroundings even in the 0.5–5 bar pressure range [*Showman and Ingersoll*, 1998]. Thus, while it is probable that the downdraft hypothesized to exist in a 5-μm hot spot region must be mechanically forced, the nature of the forcing is uncertain. R. D. Baker and G. Schubert (Deep convective entrainment in Jupiter's atmosphere: A mechanism for hot spot formation, submitted to *Icarus*, 1998) have proposed that penetrative convection can entrain the dry, cloud-free stable atmosphere originally located above the cloud tops into the deep Jovian atmosphere. The process involves merging convective downdrafts that trap dry stable atmosphere between them and drag it downward, thereby forcing less dense gas downward into the atmosphere. Basically, convective penetration of the overlying stable region mixes some of that atmosphere downward into the deeper convective part of the atmosphere. The basic convection can be moist convection in an atmosphere with approximately solar or larger water abundance, but if that convection is sufficiently vigorous, it could entrain dry atmosphere from above the cloud tops downward. A similar process may occur in Earth's atmosphere, with tropospheric convection mixing stable air from the stratosphere down into the troposphere. If convective entrainment of overlying stable atmosphere is the cause of the 5-μm hot spots, then it might account for the multitude and spacing of hot spots around Jupiter's equator by the regularity and repetition of convective elements. The present observations of large-scale turbulence in the descent velocity are consistent with the convective entrainment hypothesis.

8.6. Implications of Observed Winds

The altitude profile of Jupiter's eastward zonal winds at the probe entry site was measured by the Doppler frequency shift of the probe telemetry signal received by the orbiter [*Atkinson et al.*, 1996, 1997], by the accelerometers on the ASI [*Seiff et al.*, 1997b], and by the Doppler shift of the probe telemetry signal received directly by the VLA on Earth [*Folkner et al.*, 1997]. The wind speeds determined from the VLA observations were limited to pressures less than about 4 bars by signal absorption in Jupiter's atmosphere. The three determinations essentially agree in showing prograde winds increasing downward from the cloud tops to about the 4 bar level, below which they are approximately constant at ~200 m/s between 4 and 17 bars.

The persistence of the large zonal wind speeds to the maximum depths probed, well below the pressure levels at which absorption of solar energy occurs, suggests that the zonal winds below the cloud levels are not thermal winds driven by the latitudinal gradient of solar heating directly in the atmosphere. Instead, the Galileo zonal wind determinations appear to imply a deep origin for the winds. One such source is the deep convection that transfers much of Jupiter's internal heat to the surface. Another possibility is the suggestion of *Ioannou and Lindzen* [1994] that tides raised in a slightly stable Jovian interior by Jupiter's moon Io force the zonal winds.

Busse [1970, 1976] first suggested that a multilayered structure of columnar convection rolls might produce the zonal jets in Jupiter's atmosphere through nonlinear interactions among the rolls. Convection in the rapidly rotating Jovian interior is assuredly more temporally and spatially complex than a simple set of quasi-steady columnar convection rolls. In fact, the Rayleigh number and the Taylor number are so large that internal Jovian convection should be strongly turbulent. Nevertheless, recent numerical models of rapidly rotating convection in Jovian-like spherical shells [*Sun et al.*, 1993; *Glatzmaier and Olson*, 1993] and laboratory simulations of the process [*Manneville and Olson*, 1996], though not carried out for completely realistic Jupiter parameters, lend support to the viability of the convection hypothesis as the drive for the deep-seated zonal winds on Jupiter. *Zhang and Schubert* [1996] have shown that even if there are radiative and nonconvective layers in the outer part of the Jovian interior, zonal winds driven by deep convection would penetrate through the outer nonconvective layers to the visible surface. Though more effort is required in model simulations to approach realistic values of the parameters governing convection in Jupiter's interior (in particular, the models have yet to produce the equatorial prograde winds of the Jovian atmosphere), deep convection appears to be the most plausible drive for the strong eastward winds experienced by the Galileo probe as it descended through Jupiter's atmosphere. Undoubtedly, the deep-seated, convectively driven zonal winds near Jupiter's visible surface are modified by instabilities and waves associated with solar heating that give rise to features such as the Red Spot and the white ovals whose dynamics may be controlled by shallow-layer processes.

Appendix A: Ablation Detectors and Measurements

The probe heat shield thickness distribution was designed to provide about a 50% safety margin relative to preflight recession predictions for a nominal entry velocity of 47.8 km/s at a flight path angle −8.6° into an atmosphere containing 89% H_2 and 11% He [*Talley*, 1984]. This margin was believed to be adequate for probe survival under a worst-case scenario of steep entry at −10.0° into a "cool-heavy" atmosphere containing 25% He.

The surface recession experienced during entry was measured by ablation detectors, 1 mm diameter rods bonded into holes drilled through the heat shield. Each rod contained three insulated coaxial electrical conductors. Two of the components were low-resistance current-return leads; the third was a helical coil of platinum-tungsten wire, closely wound to produce a resistance of about 540 ohms/cm of axial length. During hypersonic entry, when the sensor's outer tip reached a temperature >800–900 K, the insulating layers pyrolyzed to form a conductive char. This completed the circuit for electric current to pass through the device. The current was provided by a precision, constant-current supply. Voltage drop through the helical coil was a measure of the unablated rod length. Experiments showed that the heat shield and embedded sensor ablate together and the sensor develops only a thin char layer at the heated surface. Therefore the voltage drop in the sensor is a direct measure of the local heat shield thickness. Sensor calibrations, in ohms/cm, were individually determined for each sensor prior to flight from measurements of sensor length and resistance.

The sensors were designed to provide a recession measurement accuracy of ±0.127 cm. This accuracy was demonstrated in high-energy ground tests of sensors bonded into the heat shield carbon phenolic material. During Jupiter entry, sensor performance was compromised by an extraneous signal which introduced oscillations at the probe spin frequency into the first half of the data and prevented definition of precise voltage biases for the sensors at the start of entry. (The extraneous signal is believed to have been generated by conductors cutting the planet's magnetic field lines.) The bias range of +0 to −5 counts measured during cruise checkouts was therefore as-

sumed for all sensors. This bias uncertainty increased the total recession uncertainty to ±0.25 cm on the nose cap and to ±0.15 cm on the frustum and base.

To construct the heat shield external shape as a function of time, curves were fit to the data from the individual sensors as functions of time. These provided six points on the forebody heat shield surface at any given time. The shape of the ablated conical section at any time was then constructed as a series of three conical frusta connecting the four frustum points. The last frustum section was extended toward the base and truncated at the measured base radius. The nose was assumed to remain spherical. Its radius was defined as a function of time by the stagnation region ablation measurements and an imposed requirement that the nose remain tangent to the first frustum section.

Since the afterbody mass loss and forebody pyrolysis were not measured, their histories were estimated. The aft mass loss and uncertainty were scaled as fixed fractions of the forebody ablative mass loss, based on past experience with similar configurations. The forebody pyrolysis mass loss and uncertainty were increased linearly from zero at −112 s (near peak heating or peak mass loss rate, Figure 3) to 1.5 ± 0.5 kg at −92 s (postablation).

Uncertainty in the heat shield mass loss, estimated as ±8.7 kg, includes uncertainty in the aft-cover mass loss and, in that, by pyrolysis. Further information on the heat shield recession measurements and their interpretation may be found in the work by *Milos* [1997].

Appendix B: Pressure Sensor Thermal Corrections

The calibrations of the pressure sensors varied slightly (tenths of a percent) with temperature within the specified operating range, −20 to +50°C. We therefore planned to apply temperature-dependent calibrations to the data and, to support this, recorded pressure sensor temperatures every 64 s during Jupiter descent. Resistance thermometers were mounted in the base of each pressure cell. At the start of descent, these sensors were at the preentry cruise temperature, −1.5°C. Within 700 s, they reached an unexpected −49°C, then increased at ~4.3°C/min to 118°C at end of mission (Figure A1), thus exceeding both the intended upper and lower limits.

Temperatures were transmitted from only the most sensitive sensor on line. At pressures between 0.5 and 4 bars, this was p_2; above 4 bars, it was p_3. The transition occurred at ~960 s. At the changeover there was a small discontinuity in the slope, dT_p/dt, which indicated that p_3 had not become quite as cold as p_2. This was consistent with the fact that the p_2 insulation envelope was pushed into the probe wall multilayer insulation, while p_3 cleared the wall insulation by ~1/2 cm. The minimum p_3 temperature was estimated to be −43°C, as shown.

Temperatures in the external Jovian atmosphere are also shown in Figure A1. Note that the sensor temperature rate reversed essentially where sensor and atmosphere temperatures crossed. Thus it appears that the sensors were effectively responding to outside atmosphere temperatures. A clear explanation of the probe thermal experience on Jupiter has not yet been put forward [*Mischel et al.*, 1997], but from the above evidence, it appears that the outside atmosphere was circulating freely within the vented probe.

The thermal equilibrium calibrations were extrapolated as shown in Figure A2 for the p_2 sensor. The symbols are cali-

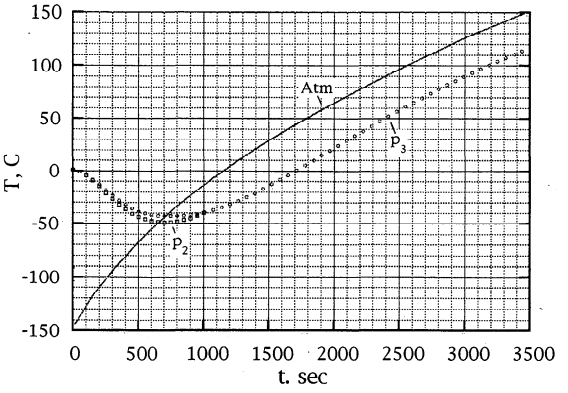

Figure A1. Temperatures measured within the pressure sensors in descent. The sensors cooled by 50°C in the first 700 s, then warmed to 118°C at the end of mission. The temperatures of the outside atmosphere are shown for comparison. At T_{min}, $T_{atm} = T_{sensor}$, as would be expected if the sensor temperature were driven by the outside atmosphere temperature.

bration data points taken over a period of several years. The upper graph shows the effect of temperature on the sensor sensitivity, or scale factor in mbar/mV = b/v. Note the highly expanded vertical scale. Scale factor was nearly independent of temperature in calibrations from −20° to +50°C. The J. A. Tavis (Acceptance test report, Galileo flight pressure sensors, personal communications, 1980) factory calibration, taken in 1980 before the sensor had aged into its final state, showed a scale factor constant within 0.1% over a temperature range from −35° to +62°C. Note also the stability of the scale factor from 1983 to 1985. In reducing the data, scale factor was assumed constant at 0.806 mbar/mV from 0° to −50°C, the value observed in 1985, with uncertainty ~1 part in 800, or 0.125%.

Extrapolations to −50°C of the sensor offset, the signal at zero pressure, are shown at the bottom of Figure A2. The

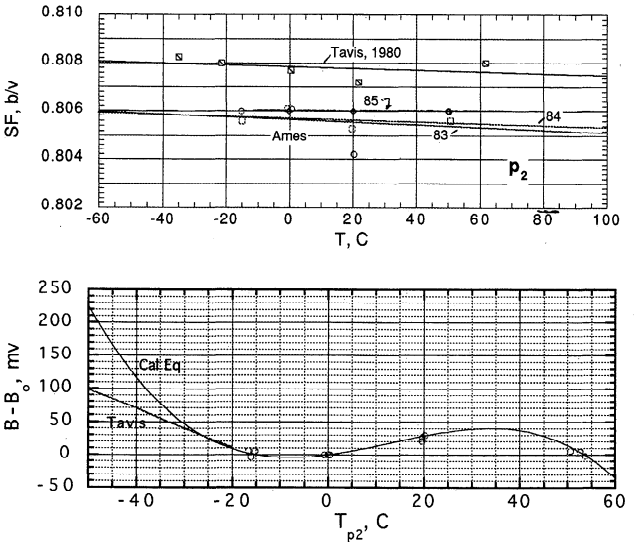

Figure A2. Extrapolations to the calibration data for the 4-bar range pressure sensor to temperatures encountered in descent. Scale factor is at the top, offset at the bottom. Two extrapolations considered for offset are shown. That labeled Cal Eq was applied to produce results shown in the text.

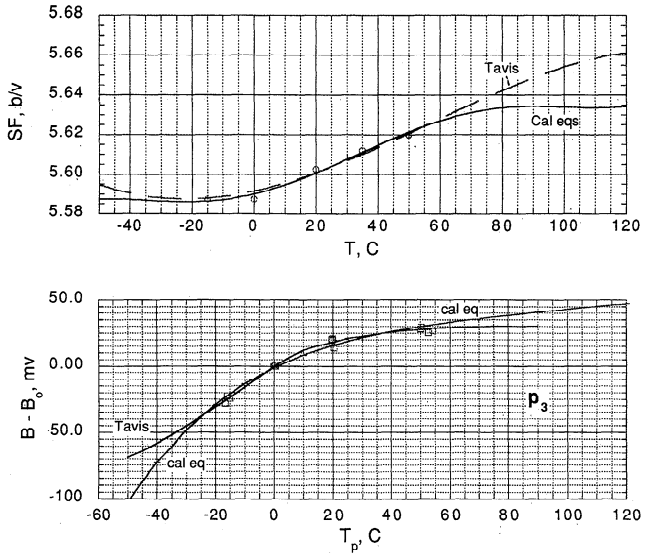

Figure A3. Extrapolations to the calibration data for the 28-bar pressure sensor. Two offset extrapolations are again shown, which may bracket the possible characteristics. The larger offset, labeled cal eq, was used to reduce the data.

upper extrapolation extends the polynomial fit to the calibration data between 54° and −16°C to −50°C. The extrapolation by J. A. Tavis (personal communication, 1996), whose company designed and manufactured the sensors, was based on calculated changes in the offset temperature compensation network and linear extrapolation of the sensor output variations over the measured range, from −30° to +60°C. The maximum difference between the two extrapolations, at −49°C, is 113 ± 50 mV equivalent to 90 ± 40 mbar. This is the dominant uncertainty in the p_2 data. The sensor was near this temperature at pressure levels between 2.5 and 4 bars. The extrapolation by use of the calibration equations results in better agreement with the p_3 data below 4 bars and gives a smaller deviation from an adiabatic atmosphere than does the Tavis extrapolation, and has been used in calculating p_2 values reported herein. Extrapolations to $T > 50$°C were unnecessary for this sensor, since it was on line only between sensor temperatures of 0° and −49°C.

Figure A3 shows the thermal equilibrium calibration data for the p_3 sensor, along with curve fits and extrapolations. The total variation of scale factor (upper graph) was ~1%, and the extrapolations did not entail significant risk. The calibration equation extrapolation and the measured p_2 and p_3 temperatures were used in deriving the data presented. The scale-factor extrapolations differed by 0.5% at 118°C and 0.15% at −50°C. In the offset extrapolations (lower graph) the difference between the two extrapolations at −49°C is 34 mV, equivalent to 190 mbar, a significant uncertainty at 2.5 bars. This uncertainty goes to zero at 1300 s, or 5.7 bars (see Figures A1 and 9b). At 100°C the offset uncertainty between plausible extremes (not shown) is 30 mV, or 170 mbar, which is 0.8% of the atmospheric pressure, 19 bars. The extrapolation uncertainty is thus most serious around 2–4 bars for both sensors, where the p_2 uncertainty could be as much as 100 mbar. Estimated uncertainties are shown in Table 4.

The sensors were electronically compensated to produce small changes in offset, or zero reading, over the intended operating range, −20° to +50°C. Outside of this range, offsets can change more rapidly, as demonstrated in tests of the engineering unit and flight spare pressure sensors, which were recalibrated after the encounter at temperatures from −50° to +70°C. (Tests were terminated at 70°C to avoid possible damage to the sensors.) Because sensor calibrations differ from unit to unit, these test results could not be directly applied to the flight sensors, but the kind of offset variations observed was consistent with the extrapolations shown in Figures A2 and A3.

Uncertainty was also introduced by high rates of change of sensor temperatures. We had specified a limit of 1°C/min as a science requirement. The actual maximum cooling rate was 7.3°C/min (p_2 sensor at 200 s). Above 4 bars, the p_3 sensor heating rate was ~4°C/min. With their temperatures changing rapidly, the sensors were not in thermal equilibrium, which affected their offsets or zero readings. We made offset corrections based on tests of the flight sensors made in 1985 at temperature rates from −1° to +3°C/min, the highest expected based on the probe descent pressure-temperature test in December 1983. Extrapolated laboratory results thus provided a basis for temperature rate corrections to the flight data, although a large extrapolation was required in the cooling direction.

The calibration sensitivities of the flight sensors to temperature rate were measured in a helium environment in 1984 and 1985. Temperature rates were measured both in the chamber and by the sensor internal thermometers. Tests at several pressures showed that scale factors were unaffected by temperature rate. Offset deviations with temperature rate are shown in Figure A4. They were approximately linear but exhibited hysteresis with increasing and decreasing temperature. (The hysteresis deviation from linearity indicates a dependence on the second derivative of temperature with time.) Sensitivities of ~18 mV/(°C/min) (equivalent to 15 mbar/(°C/min)) were measured for p_2, and 53 mbar/(°C/min) for p_3. The line through the data was extended to the maximum heating rates encountered in flight, −7.3° and +4.4°C/min. Based on the linear slope, the maximum p_2 correction was −110 mbar at 1.2 bars, and the maximum p_3 correction +235 mbar at 10 bars.

To investigate the validity of linear extrapolation and to define the hysteresis loops at temperature rates encountered in

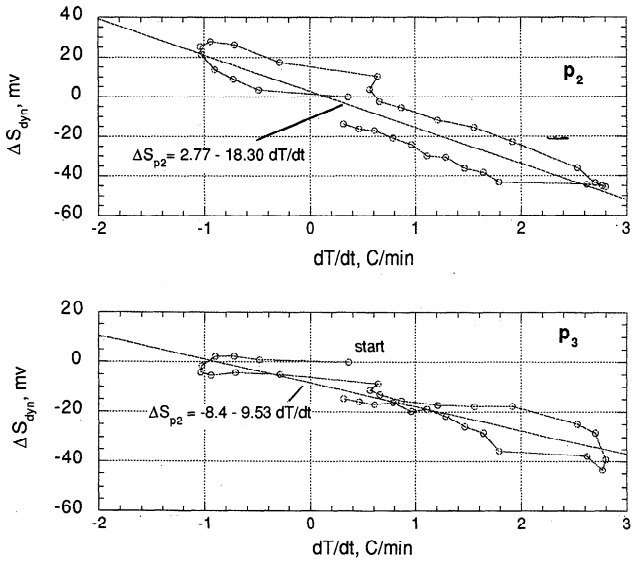

Figure A4. Flight sensor calibrations for temperature-rate sensitivity, performed in 1984 and 1985.

flight, engineering unit and flight spare sensors were exposed to the flight temperature rates in a thermal simulation, which included control of both gas and shelf temperatures, with the sensors mounted on a simulated electronics housing. Test parameters were controlled to duplicate sensor internal temperature histories as closely as possible. This was substantially achieved as shown in Figure A5 for test 17 of the engineering unit. Note the similarity of the temperature profile to that in Figure A1. Tests were terminated at 70°C to avoid possible permanent damage to the sensors. Test temperature rates, positive and negative, slightly exceeded those experienced in flight. Dynamic thermal response of the engineering unit sensor is shown in Figure A6. To allow for individual sensor differences in temperature rate sensitivity, only the hysteresis characteristics were taken from these tests. Basic linear sensitivities of the flight units were based on data of Figure A4.

The p_2 corrections for temperature rate, including hysteresis, ranged from −110 mbar at 1.4 bars to +12 mbar at 3.9 bars; p_3 corrections, from −150 mbar at 5 bars to +310 mbar at 13 bars. The uncertainty in these corrections may be approximately ±20%, equivalent to ±22 mbar in p_2 near 1.4 bars (±1.5%). The total correction applied to p_2 data near 2 bars for the temperature and temperature rate extrapolations was −190 mbar. For p_3 the assumed ±20% uncertainty in the temperature rate correction corresponds to pressure uncertainty of ±30 mbar at 5 bars (±0.6%) to ±60 mbar at 13 bars (0.4%).

Table 4 summarizes the uncertainties in pressure measurement at nine pressure levels, resulting from the probe internal temperature variations. It shows the contributions of three sources of uncertainty and the rss combined uncertainty. The scale factor uncertainty is never larger than 1 count, which is the resolution uncertainty. The offset uncertainty shown is the difference between the Tavis and calibration-equation extrapolations at the given sensor temperature (probably an overestimate). The temperature rate uncertainty shown is 20% of the linear temperature rate correction. The combined formal error is always smaller for p_2 than for p_3 below 4 bars. The peak percentage uncertainty is 2% at 0.5 bar, although this uncertainty is constrained by the p_1 data just below 0.5 bar. Other p_2 percentage uncertainties are 1.8% at 1 bar, 0.65% at 2 bars, 2.3% at 3 bars, and 0.95% at 4 bars. The disagreement between p_2 and p_3 is well within their combined estimated uncertainty, rising to this level around 2 bars, probably as a result of inexact representation of the effects of temperature rate during the period of decreasing cooling rate. Above 4 bars, the formal error is generally <1%, reaching 1.04% at 20 bars. This does not ensure accurate lapse rates, however, since the corrections and the uncertainties are functions of time and hence of pressure and altitude. Also, there is always the possibility that one or more of the above assumptions and interpretations is optimistic.

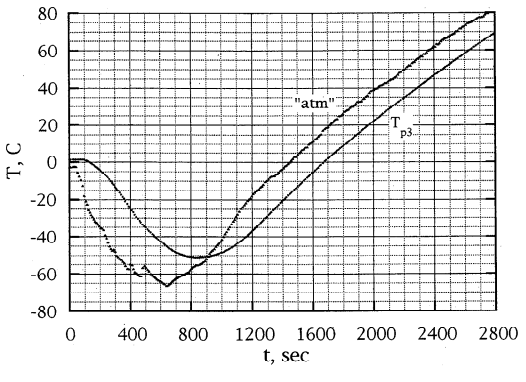

Figure A5. Example of temperature simulation achieved in postencounter testing of engineering and flight spare sensors.

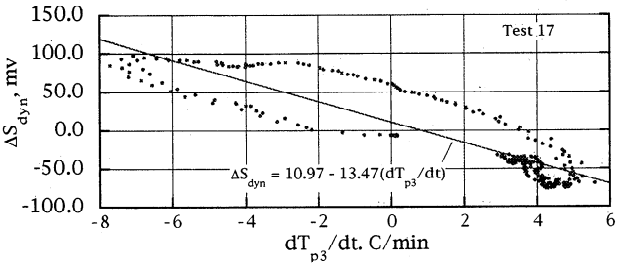

Figure A6. Response of the engineering unit high-range pressure sensor to the temperature environment of Figure A5. These data support the validity of simple extension of the data in Figure A4 to a cooling rate of −7.5°C/min. They also illustrate and were used to define the sensor response hysteresis for the flight sensor corrections.

Acknowledgments. The authors gratefully acknowledge the assistance of many individuals in the preparation of this experiment, including ASI lead engineers Joseph E. Lepetich and Layton Yee, probe instrument manager Edwin Tischler, probe test engineer Charles Sobeck, and our colleague S. C. Sommer, all of Ames Research Center; test engineer Jerry Wang of Boeing Technical Services, formerly at Ames Research Center; accelerometer engineers Daniel McCollum and John Lewis of Bell Aerospace; and electronics designer Jose Padilla and software engineer Rick Rothe, then at Martin Marietta Aerospace. We also thank Peter Gierasch for use of his code for calculating the adiabatic lapse rates of the atmosphere with various assumptions for the ortho-para hydrogen model.

References

Allison, M., Planetary waves in Jupiter's equatorial atmosphere, *Icarus*, *83*, 282–307, 1990.

Allison, M., and A. D. Del Genio, Richardson number constraints for the Jupiter and outer planet wind regime, *Geophys. Res. Lett.*, *22*, 2957–2960, 1995.

Appleby, J. F., and J. S. Hogan, Radiative-convective equilibrium models of Jupiter and Saturn, *Icarus*, *59*(3), 336–366, 1984.

Atkinson, D. H., J. B. Pollack, and A. Seiff, Galileo Doppler measurements of the deep zonal winds at Jupiter, *Science*, *272*, 842–843, 1996.

Atkinson, D. H., A. P. Ingersoll, and A. Seiff, Deep winds on Jupiter as measured by the Galileo probe, *Nature*, *388*, 649–650, 1997.

Atkinson, D. H., J. B. Pollack, and A. Seiff, The Galileo Doppler wind experiment: Measurement of the deep zonal winds on Jupiter, *J. Geophys. Res.*, this issue.

Atreya, S. K., T. M. Donahue, B. R. Sandel, A. L. Broadfoot, and G. R. Smith, Jovian upper atmospheric temperature measurement by the Voyager 1 UV spectrometer, *Geophys. Res. Lett.*, *6*(10), 795–798, 1979.

Atreya, S. K., M. H. Wong, T. Owen, H. Niemann, and P. Mahaffy, Chemistry and clouds of the atmosphere of Jupiter: A Galileo perspective, in *Three Galileos: The Man, The Spacecraft, The Telescope*, edited by J. Rahe et al., pp. 249–260, Kluwer Acad., Norwell, Mass., 1997.

Batchelor, G. K., *An Introduction to Fluid Dynamics*, Cambridge Univ. Press, New York, 1967.

Beebe, R. F., A. A. Simon, and L. F. Huber, Comparison of Galileo probe and Earth-based translation rates of Jupiter's equatorial clouds, *Science*, *272*, 841–842, 1996.

Bjoraker, G. L., H. P. Larson, and V. G. Kunde, The abundance and

distribution of water vapor in Jupiter's atmosphere, *Astrophys. J.*, *311*(2), 1058–1072, 1986.

Busse, F. H., Thermal instabilities in rapidly rotating systems, *J. Fluid Mech.*, *44*, 441–460, 1970.

Busse, F. H., Simple model of convection in the Jovian atmosphere, *Icarus*, *29*, 250–260, 1976.

Carlson, R., et al., Near-infrared spectroscopy and spectral mapping of Jupiter and the Galilean satellites: Results from Galileo's initial orbit, *Science*, *274*, 385–388, 1996.

Chapman, D. R., An approximate analytical method for studying entry into planetary atmospheres, *NACA Tech. Note*, *TN 4276*, 1958.

Clarke, J. T., M. K. Hudson, and Y. L. Yung, The excitation of the far ultraviolet electroglow emissions on Uranus, Saturn, and Jupiter, *J. Geophys. Res.*, *92*, 15,139–15,147, 1987.

Eshleman, V. R., G. L. Tyler, G. E. Wood, G. F. Lindal, J. D. Anderson, and G. S. Levy, Radio science with Voyager 1 at Jupiter: Preliminary profiles of the atmosphere and ionosphere, *Science*, *204*, 976–978, 1979.

Festou, M. C., S. K. Atreya, T. M. Donahue, B. R. Sandel, D. E. Shemansky, and A. L. Broadfoot, Composition and thermal profiles of the Jovian upper atmosphere determined by the Voyager ultraviolet stellar occultation experiment, *J. Geophys. Res.*, *86*(A7), 5715–5725, 1981.

Flasar, F. M., and P. J. Gierasch, Mesoscale waves as a probe of Jupiter's deep atmosphere, *J. Atmos. Sci.*, *43*, 2683–2707, 1986.

Folkner, W. M., R. A. Preston, J. S. Border, J. Navarro, W. E. Wilson, and M. Oestreich, Earth-based radio tracking of the Galileo probe for Jupiter wind estimation, *Science*, *275*, 644–646, 1997.

Folkner, W. M., R. Woo, and S. Nandi, Ammonia abundance in Jupiter's atmosphere derived from the attenuation of the Galileo probe's radio signal, *J. Geophys. Res.*, this issue.

General Electric Co., Final test report for the Galileo probe system drop test number 2, *Doc. 83SDS2148*, Re-entry Systems Operations, Philadelphia, Pa., Oct. 1983.

Gierasch, P. J., and B. J. Conrath, Energy conversion processes in the outer planets, in *Advances in Planetary Meteorology*, edited by G. Hunt, pp. 121–146, Cambridge Univ. Press, New York, 1985.

Gladstone, G. R., M. Allen, and Y. L. Yung, Hydrocarbon photochemistry in the upper atmosphere of Jupiter, *Icarus*, *119*, 1–52, 1996.

Glatzmaier, G. A., and P. Olson, Highly supercritical thermal convection in a rotating spherical shell: Centrifugal vs. radial gravity, *Geophys. Astrophys. Fluid Dyn.*, *70*(1-4), 113–136, 1993.

Guillot, T., D. Gautier, G. Chabrier, and B. Mosser, Are the giant planets fully convective?, *Icarus*, *112*, 337–353, 1994.

Haas, B. L., and F. S. Milos, Simulated rarified entry of the Galileo probe into the Jovian atmosphere, *J. Spacecraft Rockets*, *32*(3), 398–403, 1995.

Hanel, R. A., B. J. Conrath, L. W. Herath, V. G. Kunde, and J. A. Pirraglia, Albedo, internal heat, and energy balance of Jupiter: Preliminary results of the Voyager infrared investigation, *J. Geophys. Res.*, *86*(A10), 8705–8712, 1981.

Hilsenrath, J., C. Beckett, W. S. Benedict L. Fano, H. J. Hoge, J. D. Musi, E. L. Nuttall, and Y. S. Touloukian, *Tables of Thermodynamic and Transport Properties of Air, Argon, Carbon Dioxide, Carbon Monoxide, Hydrogen, Nitrogen, Oxygen, and Steam*, Pergamon, Tarrytown, New York, 1960.

Hubbard, W. B., Thermal models of Jupiter and Saturn, *Astrophys. J.*, *155*, 157–161, 1969.

Hunt, G. E., B. J. Conrath, and J. A. Pirraglia, Visible and infrared observations of Jovian plumes during the Voyager encounter, *J. Geophys. Res.*, *86*(A10), 8777–8781, 1981.

Hunten, D. M., and A. J. Dessler, Soft electrons as a possible heat source for Jupiter's thermosphere, *Planet. Space Sci.*, *25*, 817, 1977.

Ingersoll, A. P., G. Munch, G. Neugebauer, D. J. Diner, G. S. Orton, B. Schupler, M. Schroeder, S. C. Chase, R. D. Ruiz, and L. M. Trafton, Pioneer 11 infrared radiometer experiment: The global heat balance of Jupiter, *Science*, *188*, 472–473, 1975.

Ingersoll, A. P., R. Beebe, J. L. Mitchell, G. W. Garneau, G. M. Yagi, and J. Müller, Interaction of eddies and mean zonal flow on Jupiter as inferred from Voyager 1 and 2 images, *J. Geophys. Res.*, *86*, 8733–8743, 1981.

Intrieri, P. F., and D. B. Kirk, High-speed aerodynamics of several blunt-cone configurations, *J. Spacecraft Rockets*, *24*(2), 127, 1987.

Ioannou, P. J., and R. S. Lindzen, Gravitational tides in the outer planets, I, Implications of classical tidal theory, *Astrophys. J.*, *406*, 252–265, 1993a.

Ioannou, P. J., and R. S. Lindzen, Gravitational tides on Jupiter, II, Interior calculations and estimation of the tidal dissipation factor, *Astrophys. J.*, *406*, 266–278, 1993b.

Ioannou, P. J., and R. S. Lindzen, Gravitational tides on Jupiter, III, Atmospheric response and mean flow acceleration, *Astrophys. J.*, *424*, 1005–1013, 1994.

Kliore, A. J., and P. M. Woiceshyn, Structure of the atmosphere of Jupiter from Pioneer 10 and 11 radio occultation measurements, in *Jupiter*, edited by T. Gehrels, pp. 216–237, Univ. of Ariz. Press, Tucson, 1976.

Kunde, V., R. Hanel, W. Maguire, D. Gautier, J. P. Baluteau, A. Marten, A. Chedin, N. Husson, and N. Scott, The tropospheric gas composition of Jupiter's north equatorial belt (NH_3, PH_3, CH_3D, GeH_4, H_2O) and the Jovian D/H isotopic ratio, *Astrophys. J.*, *263*, 443–467, 1982.

Lewis, J. S., The clouds of Jupiter and the NH_3-H_2O and NH_3-H_2S systems, *Icarus*, *10*, 365–378, 1969.

Limaye, S. S., H. E. Revercomb, L. A. Sromovsky, R. J. Krauss, D. A. Santek, and V. E. Suomi, Jovian winds from Voyager 2, I, Zonal mean circulation, *J. Atmos. Sci.*, *39*(7), 1413–1432, 1982.

Lindal, G. F., et al., The atmosphere of Jupiter: An analysis of the Voyager radio occultation measurements, *J. Geophys. Res.*, *86*, 8721–8727, 1981.

Lindzen, R. S., Turbulence and stress owing to gravity wave and tidal breakdown, *J. Geophys. Res.*, *86*, 9704–9714, 1981.

Manneville, J. B., and P. Olson, Banded convection in rotting fluid spheres and the circulation of the Jovian atmosphere, *Icarus*, *122*(2), 242–250, 1996.

Mason, E. A., and T. R. Marrero, The diffusion of atoms and molecules, in *Advances in Atomic and Molecular Physics*, vol. 6, edited by D. R. Bates and I. Esterman, pp. 155–232, Academic, San Diego, Calif., 1970.

Milos, F. S., Galileo Probe Heat Shield Ablation Experiment, *J. Spacecraft Rockets*, *34*(6), 705–713, 1997.

Mischel, B., T. Rust, and F. Linckhorst, Galileo probe descent postflight thermal correlation analysis, Am. Inst. of Aeronaut. and Astronaut., New York, 1997.

Niemann, H. B., et al., The Galileo probe mass spectrometer: Composition of Jupiter's atmosphere, *Science*, *272*, 846–849, 1996.

Niemann, H. B., et al., The composition of the Jovian atmosphere as determined by the Galileo probe mass spectrometer, *J. Geophys. Res.*, this issue.

Nishida, A., and Y. Watanabe, Joule heating of the Jovian ionosphere by corotation enforcement currents, *J. Geophys. Res.*, *86*, 9945–9952, 1981.

Ortiz, J. L., G. S. Orton, A. J. Friedson, S. T. Stewart, B. M. Fisher, and J. R. Spencer, Evolution and persistence of 5-μm hot spots at the Galileo probe entry latitude, *J. Geophys. Res.*, this issue.

Orton, G., and A. P. Ingersoll, Pioneer 10 and 11 and ground-based infrared data on Jupiter: The thermal structure and He/H_2 ratio, in *Jupiter*, edited by T. Gehrels, pp. 206–215, Univ. of Ariz. Press, Tucson, 1976.

Orton, G., et al., Earth-based observations of the Galileo probe entry site, *Science*, *272*, 839–840, 1996.

Orton, G., et al., Characteristics of the Galileo probe entry site from Earth-based remote sensing observations, *J. Geophys. Res.*, this issue.

Owen, T., and R. J. Terrile, Colors on Jupiter, *J. Geophys. Res.*, *86*(A10), 8797–8814, 1981.

Ragent, B., D. S. Colburn, K. A. Rages, T. C. D. Knight, P. Avrin, G. S. Orton, P. A. Yanamandra-Fisher, and G. W. Grams, The clouds of Jupiter: Results of the Galileo Jupiter Mission Probe Nephelometer Experiment, *J. Geophys. Res.*, this issue.

Roques, F., et al., Neptune's upper stratosphere, 1983–1990: Ground-based stellar occultation observations, III, Temperature profiles, *Astron. Astrophys.*, *288*, 985–1011, 1994.

Seiff, A., and T. C. D. Knight, The Galileo probe Atmosphere Structure Instrument, *Space Sci. Rev.*, *60*, 203–232, 1992.

Seiff, A., D. E. Reese, S. C. Sommer, D. B. Kirk, E. E. Whiting, and H. B. Niemann, PAET, An entry probe experiment in the Earth's atmosphere, *Icarus*, *18*(4), 525–563, 1973.

Seiff, A., D. B. Kirk, R. E. Young, R. C. Blanchard, J. T. Findlay, G. M. Kelly, and S. C. Sommer, Measurements of thermal structure and thermal contrasts in the atmosphere of Venus and related dynamical observations: Results from the four Pioneer Venus probes, *J. Geophys. Res.*, *85*(A13), 7903–7933, 1980.

Seiff, A., et al., Structure of the atmosphere of Jupiter: Galileo probe measurements, *Science*, *272*, 844–845, 1996a.

Seiff, A., E. Venkatapathy, B. Haas, and P. F. Intrieri, Galileo probe aerodynamics, *Pap. AIAA-96-2451*, Am Inst. of Aeronaut. and Astronaut., Washington, D. C., 1996b.

Seiff, A., D. B. Kirk, T. C. D. Knight, L. A. Young, F. S. Milos, E. Venkatapathy, J. D. Mihalov, R. C. Blanchard, R. E. Young, and G. Schubert, Thermal structure of Jupiter's upper atmosphere derived from the Galileo probe, *Science*, *276*, 102–104, 1997a.

Seiff, A., R. C. Blanchard, T. C. D. Knight, G. Schubert, D. B. Kirk, D. Atkinson, J. D. Mihalov, and R. E. Young, Wind speeds measured in the deep Jovian atmosphere by the Galileo probe accelerometer, *Nature*, *388*, 650–652, 1997b.

Showman, A., and A. P. Ingersoll, Interpretation of Galileo probe data and implications for Jupiter's dry downdrafts, *Icarus*, *132*, 205–220, 1998.

Smith, B. A., et al., The Jupiter system through the eyes of Voyager I, *Science*, *204*, 951–972, 1979.

Smith, M. D., and P. J. Gierasch, Convection in the outer planet atmospheres including ortho-para hydrogen conversion, *Icarus*, *116*, 159–179, 1995.

Smoluchowski, R., Origin and structure of Jupiter and its satellites, in *Jupiter*, edited by T. Gehrels, pp. 3–21, Univ. of Ariz. Press, Tucson, 1976.

Sromovsky, L. A., F. A. Best, A. D. Collard, P. M. Fry, H. E. Revercomb, R. S. Freedman, G. S. Orton, J. L. Hayden, M. G. Tomasko, and M. T. Lemmon, Solar and thermal radiation in Jupiter's atmosphere: Initial results of the Galileo probe net flux radiometer, *Science*, *272*, 851–854, 1996.

Sromovsky, L. A., A. D. Collard, P. M. Fry, G. S. Orton, M. T. Lemmon, M. G. Tomasko, and R. S. Freedman, Galileo probe measurements of thermal and solar radiation fluxes in the Jovian atmosphere, *J. Geophys. Res.*, this issue.

Strobel, D. F., and G. R. Smith, On the temperature of the Jovian thermosphere, *J. Atmos. Sci.*, *30*, 718–725, 1973.

Sun, Z. P., G. Schubert, and G. A. Glatzmaier, Banded surface flow maintained by convection in a model of the rapidly rotating giant planets, *Science*, *260*, 661–664, 1993.

Talley, R. N., Galileo probe deceleration module final report, *84SDS2020*, Re-entry Systems Operations, General Electric Co., Philadelphia, Pa., Jan. 1984.

Townsend, A. A., *The Structure of Turbulent Shear Flow*, 2nd ed., Cambridge Univ. Press, New York, 1976.

von Zahn, U., and D. M. Hunten, The helium mass fraction in Jupiter's atmosphere, *Science*, *272*, 849–851, 1996.

von Zahn, U., D. M. Hunten, and G. Lehmacher, Helium in Jupiter's atmosphere: Results from the Galileo Probe Helium Interferometer Experiment, *J. Geophys. Res.*, this issue.

Waite, J. H., Jr., G. R. Gladstone, W. S. Lewis, P. Drossart, T. E. Cravens, A. N. Maurellis, B. H. Mauk, and S. Miller, Equatorial X-ray emissions: Implications for Jupiter's high exospheric temperatures, *Science*, *276*, 104–108, 1997.

West, R. A., D. F. Strobel, and M. G. Tomasko, Clouds, aerosols, and photochemistry in the Jovian atmosphere, *Icarus*, *65*, 161–217, 1986.

Yelle, R. V., L. A. Young, R. J. Vervack Jr., R. E. Young, L. Pfister, and B. R. Sandel, Structure of Jupiter's upper atmosphere: Predictions for Galileo, *J. Geophys. Res.*, *101*(E1), 2149–2161, 1996.

Young, L. A., R. V. Yelle, R. E. Young, A. Seiff, and D. B. Kirk, Gravity waves in Jupiter's thermosphere, *Science*, *276*, 108–111, 1997.

Young, R. E., M. A. Smith, and C. K. Sobeck, Galileo probe: In situ observations of Jupiter's atmosphere, *Science*, *272*, 837–838, 1996.

Zhang, K., and G. Schubert, Penetrative convection and zonal flow on Jupiter, *Science*, *273*, 941–943, 1996.

Hughes Space and Communications Co., Galileo Probe Mission Operations Final Report, *HS 373-6000*, El Segundo, Calif., 1996.

D. Atkinson, Department of Electrical and Computer Engineering, University of Idaho, Moscow, ID 83844.

R. C. Blanchard, NASA Langley Research Center, Hampton, VA 23681-0001.

D. B. Kirk, Department of Physics, University of Oregon, Eugene, OR 97403.

T. C. D. Knight, 2370 South Bentwood Street, Lakewood, CO 80227.

J. D. Mihalov, F. S. Milos, A. Seiff, and R. E. Young, NASA Ames Research Center, MS 245-1, Moffett Field, CA 94035.

G. Schubert, Department of Earth and Space Sciences, University of California, Los Angeles, CA 90024-1567.

L. A. Young, Center for Space Physics, Boston University, Boston, MA 02215.

(Received September 5, 1997; revised May 6, 1998;
accepted May 26, 1998.)